Diploma Thesis

Optimization of novel thermally activated single-use valves and pumps for minimally invasive transdermal drug delivery and Lab-on-Chip applications

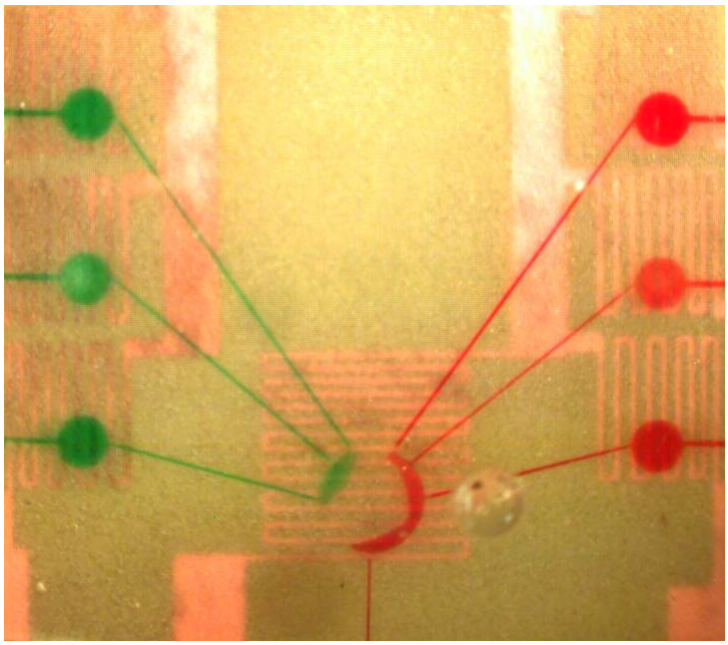

Volker Nock

IMTEK

Diploma thesis submitted in partial fulfillment of the requirements for the degree of Diploma in Engineering Sciences in the Graduate Division of the Albert-Ludwigs University of Freiburg, Germany.

Institute for Microsystem Technology IMTEK
Laboratory for Design of Microsystems
Albert-Ludwigs-University
Freiburg im Breisgau, Germany

Author Volker Nock
Matr.-Nr.: 9708430
E-Mail: volker.nock@web.de

Examiner Prof. Dr. Göran Stemme, KTH Stockholm, Microsystem Technology
Co-Examiner Prof. Dr.-Ing. Peter Woias, IMTEK Freiburg, Chair for Construction of Microsystems
Supervisor Dipl.-Ing.(FH) Björn Samel, PhD student, KTH Stockholm

Frontpage Micrograph of disposable liquid handling lab-on-a-chip (LOC) system.

Erklärung

Hiermit erkläre ich, dass ich die vorliegende Arbeit selbstständig und ohne Benutztung anderer als der angegebenen Hilfsmittel angefertigt habe und Stellen, die wörtlich oder sinngemäß aus veröffentlichten Schriften entnommen wurden, als solche kenntlich gemacht habe. Desweiteren erkläre ich, dass diese Arbeit nicht, auch nur auszugsweise, für eine andere Prüfung verwendet wurde.

Volker Nock, Stockholm, den 18 Januar 2005

TABLE OF CONTENTS

ABSTRACT

This thesis reports on the optimization of microfluidic devices based on a novel temperature sensitive elastomer composite. The composite consists of expandable microspheres confined in a polydimethylsiloxane (PDMS) matrix and allows to design highly integrated active liquid handling networks. Devices employing this composite can be fabricated entirely of low-cost materials on a wafer-level scale. Upon heating the microspheres increase their volume expanding the composite. In contrast to other approaches complicated localization of the actuator material is avoided by using embedded heat sources to geometrically define expansion.

The work presented focuses on the theoretical and experimental investigation of embedded microheater performance, based on which innovative heater designs are proposed. In addition, fluid temperature is measured during device operations.

Partial fluid entrapment during operation and resulting high alignment precision during fabrication are addressed by using specially designed heaters. Devices with microheaters based on printed circuit board (PCB) technology as thermal power source are analyzed and simulated using finite element modelling (FEM). Heater trace width and spacing are adjusted to produce custom temperature profiles. Temperature dependence of fluorescence for RhodamineB is adapted to compare fabricated heater shapes with simulation results.

The potential problem of excessive temperature increase of the fluid as a consequence of the actuation principle is investigated using fluorescence based thermometry. Direct fluid temperature measurements for typical actuation currents are performed on pure PDMS dummies and composite based active devices. An intermediate gold layer as well as custom machined PDMS observation windows are introduced for active devices to enable the measurement process. Fluid temperatures of up to 43°C on dummy devices and up to 35°C on composite based devices are measured in the fluidic system during similar operation conditions.

ZUSAMMENFASSUNG

Diese Diplomarbeit behandelt die Optimierung mikrofluidischer Komponenten auf Basis eines neuartigen, temperatursensitiven Elastomerkomposits. Das Komposit besteht aus expandierbaren Mikrokugeln eingebettet in eine Matrix aus Polydimethylsiloxane (PDMS) und erlaubt die Herstellung hochintegrierter, aktiver Netzwerke zur kontrollierten Handhabung von Flüssigkeiten. Komponenten welche das Komposit verwenden, können vollständig aus preiswerten Materialien und unter Verwendung von Waferlevel-Prozessen hergestellt werden. Bei Zuführung von Wärmeenergie nimmt das Volumen der Mikrokugeln zu und das Komposit expandiert. Im Gegensatz zu alternativen Ansätzen ist eine komplizierte Lokalisierung des Aktuatormaterials nicht notwendig, da stattdessen eingebettete Hitzequellen verwendet werden können.

Der Fokus der vorgestellten Arbeit liegt im ersten Teil auf der theoretischen und experimentellen Untersuchung der Leistungsmerkmale eingebetteter Mikroheizer und basierend darauf auf der Entwicklung neuer, innovativer Heizergeometrien. Aufbauend hierauf wird im zweiten Teil die Temperatur der Flüssigkeit während des Betriebes bestimmt.

Bedingt durch teilweises Einschliessen von Flüssigkeit während des Betriebs der Komponenten, bedurfte es bisher einer sehr hohen Justiergenauigkeit in der Montage. Gerichtet an diese Problematik werden speziell angepaßte Temperaturprofile entworfen. Hierfür werden Mikroheizer auf Leiterplattentechnologie analysiert und ihre Funktion als thermische Energiequelle mit Hilfe der Finiten Elemente Modellierung simuliert. Durch Variation von Leiterbahnbreite und Abstand innerhalb der Heizermäandern werden spezifische Temperaturprofile generiert. Die Temperaturabhängigkeit der Fluoreszenz von RhodamineB wird zur Auswertung hergestellter Heizer verwendet. Diese Ergebnisse werden mit Simulationsresultaten verglichen. Die Verwendung in einem Einweg-Lab-on-Chip System demonstriert die Tauglichkeit des entworfenen Designs.

Der zweite Teil der Arbeit richtet sich an die Messung der absorbierten Wärmeenergie der zu transportierenden Flüssigkeit als Folge des Aktuationsprinzipes. Hierfür wird anhand der Fluoreszenz-basierten Thermometrie die Temperatur der Flüssigkeit im mikrofluidischen System für typische Ansteuerströme bestimmt. Für die Messungen werden unterschiedliche passive Komponenten aus purem PDMS und aktive Komponenten auf Kompositbasis eingeführt, letztere mit Goldzwischenschicht oder Observationsöffnung. Als Höchsttemperatur unter Betrieb werden für passive bis zu 43°C und für aktive Komponenten bis zu 35°C unter jeweils vergleichbaren Voraussetzungen gemessen.

1 INTRODUCTION

"The most exciting phrase to hear in science, the one that heralds new discoveries, is not 'Eureka!' (I found it!) but 'That's funny...'"
Isaac Asimov

The ability to control gradually smaller amounts of liquids is desirable in both the fields of chemistry and biomedicine. Miniaturization by means of microsystem technology (MST) offers the possibility to meet this trend. Microfluidics, commonly referred to research into controlled handling of liquids in the μl-range and below, has therefore received growing attention from both industry and academia.

In general, the use of microsystem technology in design and fabrication of fluidic devices leads to several advantages. Among these are increase in sensitivity and in speed of analysis, as well as reduction of reagents consumed and possibly harmful by-products produced. In addition, reduced production costs associated with the use of high volume batch fabrication methods in combination with an increase in portability allow for disposable devices to become feasible.

Today application areas for microfluidic devices cover a wide spectrum. From micromixers for microreaction engineering [1,2] to inkjet print heads, from integrated polymerase chain reaction (PCR) to on-chip genotyping [3], fluidic microsystems essentially aim at a broad variety of markets. One if not the fastest growing market for microsystems today is certainly that for biomedical applications. With an increasing life expectancy in the industrialized world and a growing need to find cures for modern epidemics like HIV, big opportunities arise not only for highly integrated Lab-on-Chip (LOC) systems, but also for new drug delivery methods.

Today's existing means to get drugs into the body are not only most often rather ineffective or even disruptive, they may also be downright painful. On top of that they also prevent the introduction of a whole new range of promising drugs that can not be administered in the conventional sense. One novel alternative method with the promise to circumvent those problems is transdermal drug delivery. Hereby only the outer-most skin layer, the Stratum Corneum (SC), is transversed, avoiding tissue damage especially in the deeper, nerve carrying layers and the fluid to be delivered is pumped through the newly opened conduit by a suitable power source. Among the different methods proposed to transverse the SC [4,5], microneedles in general and side-opened out-of-plane needle arrays [6] in particular seem to be promising approaches with the least risk for tissue damage.

Both drug delivery and LOC systems require novel approaches in terms of fluid actuation, especially out of a system integration point of view. An ideal fluidic power source should be robust, biocompatible, cheap and disposable, as to name only some of the most important requirements. Various pumps have been proposed employing a diversity of actuation

principles that allow for one-shot use but usually require rather complicated packaging of the actuator material [7-9].

The work described in the following chapters relates to novel one-shot pumps and valves proposed for drug delivery and LOC systems based on an active polydimethylsiloxane (PDMS) composite. The actuation material shows both outstanding expansion behavior and greatly simplified fabrication requirements making it ideal for low-cost, disposable applications.

1.1 OBJECTIVES OF THIS DIPLOMA THESIS

The objectives of this thesis are (i) to optimize the heat field of the heaters employed for the one-shot valves and pumps based on expandable microspheres and (ii) to measure the temperatures a fluid is exposed to during typical actuation conditions.

All work was carried out at the department of Signals, Sensors and Systems (S3) Microsystem Technology Laboratory and the “Electrum” cleanroom facility, Royal Institute of Technology, Stockholm, Sweden.

1.2 OVERVIEW OVER THIS DOCUMENT

Chapter 1 includes an introduction to the background of the project and the objectives of the diploma thesis presented here, as well as an overview over the layout of this document.

In Chapter 2 a summary of the previously performed research on expandable microspheres for fluid actuation is presented in relation to this thesis. The chapter closes with a detailed description of the device problems addressed.

Chapter 3 describes the work performed to optimize the heat field of the microheaters by introducing the physical background of the actuation principle, followed by a description of the simulations, the actual fabrication process for the devices and concluded by a presentation of the results.

Chapter 4 describes the temperature measurements performed on the devices. An introduction to fluorescence-based thermometry is given, followed by the calibration procedure. Use of the method for characterization of heaters designed in the previous chapter is explained together with changes to devices necessary for measurements. Concluding the chapter measurement results for active devices are presented.

The thesis is summarized by a final conclusion to the different parts in Chapter 5. The above chapters are supplemented by an appendix containing the various heater shapes produced as well as the Matlab code used to perform the fluorescence-based temperature measurements.

2 BACKGROUND

> "*If we have learned one thing from the history of invention and discovery, it is that, in the long run - and often in the short one - the most daring prophecies seem laughably conservative.*"
> Arthur C. Clarke

In this section expandable microspheres and their applications are described. Previous work related to microspheres for the handling of liquids is summarized and the current project concerning their use as an actuator for lab-on-a-chip devices and transdermal drug delivery is introduced.

2.1 INTRODUCTION TO EXPANDABLE MICROSPHERES

EXPANCEL© microspheres are produced by Expancel (Sundsvall, Sweden), part of Surface Chemistry, a business unit of the Dutch company Akzo Nobel. Other expandable microspheres available are MICROPEARL™ Unexpanded Spheres by Sovereign Specialty Chemicals, Inc. (Chicago, USA) and ADVANCELL EM by Sekisui Chemical CO., Ltd. (Osaka, Japan).

Today, their most common areas of application are as blowing agent in for example reaction injection molding and printing inks and as weight reducer in paints and spackling material [10]. Being sold in typical amounts of several hundred kilograms their price is accordingly low for those quantities needed in microsystem applications. All following descriptions of expandable microspheres and work related to them refer to Expancel© microspheres.

Properties

The microspheres consist of a spherical thermoplastic shell and a blowing agent contained within. The shell is a copolymer of some monomers, e.g. vinylidene chloride, acrylonitrile and methylmethacrylate, enclosing a liquid hydrocarbon, usually isobutane or isopentane. Upon application of heat the shell softens and the hydrocarbon changes phase from liquid to gas, increasing the pressure inside the sphere. This leads to a dramatic increase of volume of up to more than 40 times, as shown for typical values in Figure 2.1.

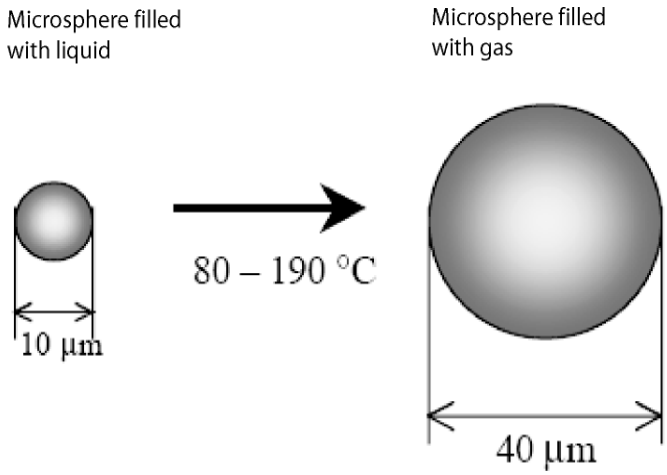

Figure 2.1: *Expansion of Expancel© microspheres for typical diameter values*

After removing the heat the shell stiffens and the sphere retains its expanded shape. If heated above temperature of maximum expansion the microspheres gradually collapse.

Expancel© microspheres are available both unexpanded as well as pre-expanded, with diameters between 5 and 40 µm and expansion temperatures ranging between 75 and 190°C depending on their grade (Figure 2.2).

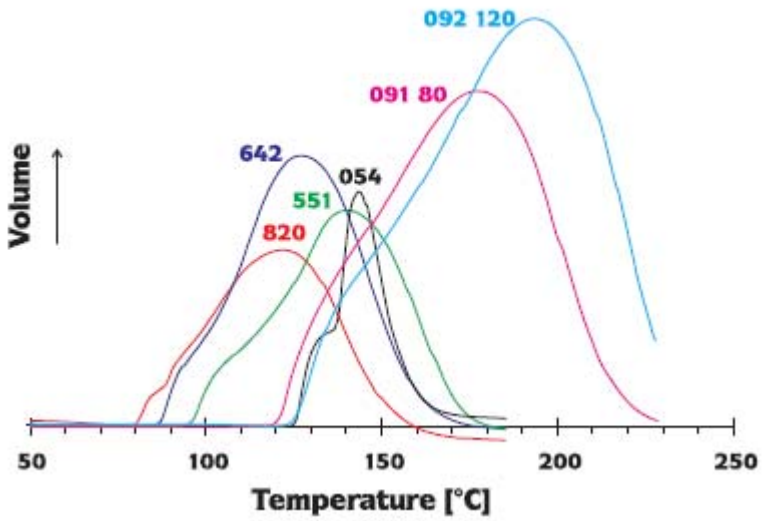

Figure 2.2: *Expansion intervals for different grades of Expancel© microspheres*

The microspheres used in the work presented here are of the grade Expancel© 820DU (where DU stands for dry unexpanded) with an expansion start temperature of T_{start} = 75-80°C and an average particle size D(0.5) = 10-16μm [11].

In general, all grades are highly resilient, can withstand numerous loading/unloading cycles without collapsing or breaking and can be used in contact with a wide range of chemicals without negative effect on their properties.

2.2 EXPANDABLE MICROSPHERES FOR THE HANDLING OF LIQUID

2.2.1 LOCALIZATION BY MECHANICAL BARRIER

The use of expandable microspheres as novel method for the handling of liquids was first introduced in [12]. By implementing a mechanical filter of high aspect ratio pillars, microspheres were localized in a channel and successfully employed as one-shot valve and one-shot pump respectively. Figure 2.3 shows the principle of operation for microsphere based valves and pumps.

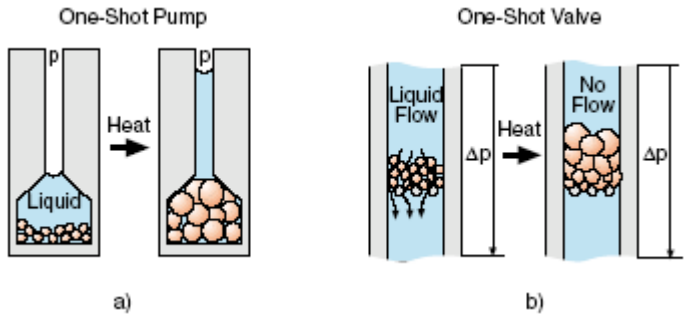

Figure 2.3: *Two concepts for liquid handling by Expancel beads, a) one-shot pump, b) normally open one-shot valve.*

Used as a pump, the setup allowed for liquid volumes in the nanoliter range to be displaced against a counter pressure of 100 kPa, while as valve it completely blocked the flow of water through a microchannel.

2.2.2 LOCALIZATION BY PHOTOLITHOGRAPHY AND SELF-ASSEMBLY

Further studies evaluated surface immobilization techniques for selective localization of microspheres in fluidic systems [13]. In contrast to mechanical barriers, photolithography and surface chemistry based self-assembly were applied to selectively arrange patterns of beads on unstructured silicon surfaces. The former was facilitated by mixing microspheres with standard photoresist followed by resist exposure and development. The latter involved the localized functionalization of the silicon surface via microcontact printing stamp with subsequent adding of an aqueous slurry of microspheres. The promising results of the work presented above instigated further investigations into the use of expandable microspheres, namely characterization of expansion behavior and introduction of a novel active composite material.

2.2.3 LOW-COST LIQUID DISPENSING DEVICE

To actually realize a dosing device with microspheres as actuator, their expansion behavior was characterized regarding excitation temperature and corresponding volume of expansion as part of a master thesis [14].

Low cost dispensing device

Resulting from these investigations, a design for a dosing pump was proposed. The fabricated device and its characterization were reported in [15]. The mechanical setup of the device consist of three basic layers (Figure 2.4),

- first a heater made in printed circuit board (PCB) technology,
- second a ring containing an expandable paste covered by a membrane,
- and last a container holding the liquid to be delivered.

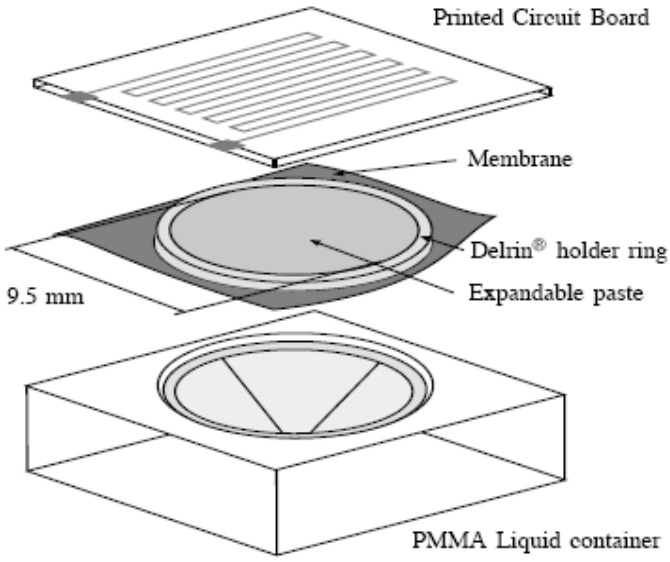

Figure 2.4: *Schematic view of device. The ring together with the membrane is clamped into the container thereby flattening the membrane.*

As opposed to mixing with water, microspheres were mixed with glycerin for this application. This was done to take advantage of the higher heat conductivity and boiling point of glycerol, avoiding evaporation effects. In addition, the mixture acquires a consistency suitable for screen printing. To prevent contamination of fluid to be dispensed, a thin flexible

vinyl membrane chemically separates liquid and expanding mixture. A conceptional view of the working principle of the pump is depicted in Figure 2.5

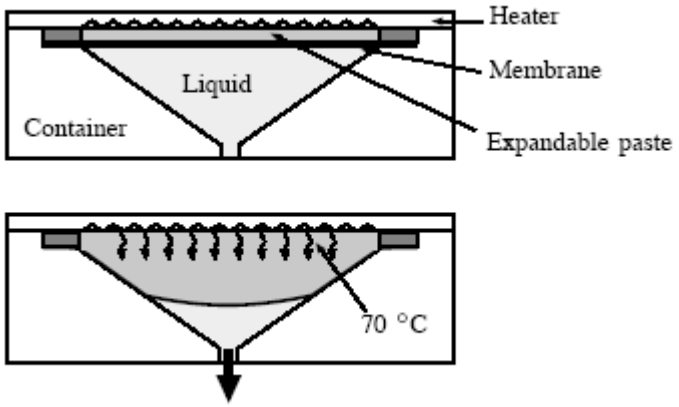

Figure 2.5: *Upon reaching 70°C paste expands, filling out the container and thereby pushing out the fluid.*

During expansion the paste itself functions as a thermal protection layer, reducing heat conduction towards the fluid. Since expansion is irreversible no valve structures are needed to prevent back-flow of fluid.

Application as low-cost dye laser dispenser

A further optimized version of the device above was presented in [16] for use as a laser dye dispenser targeted at integrated LOC applications. The pump was operated as a low flow-rate dispenser delivering a regenerating flow of 1-10ml over up to more than 10 hours, which is sufficient to prevent the dye in the laser cavity from bleaching by external optical excitation.

2.3 PDMS-XB - A NOVEL ACTIVE COMPOSITE MATERIAL

As processing of materials found in the conventional semiconductor industry is in general both expensive and time consuming, alternative materials have become increasingly popular in the fabrication of microfluidic systems. One of the most promising choices is the use of polymers due to advantageous qualities like bio-compatibility, ease of processing and reduced price. Current examples are PDMS and Cyclic Olefin Copolymer (COC/TOPAS©).

2.3.1 EXPANDABLE MICROSPHERES INCORPORATED IN PDMS

To combine the merits of microspheres as well as those of polymers a novel composite material (i.e. expandable microspheres mixed with PDMS, PDMS-XB) was introduced in [17]. For the first time microspheres were incorporated in a matrix of PDMS, giving rise to a wide range of new applications.

To fabricate the composite, Expancel 820DU microspheres are mixed with PDMS base followed by a degassing step in vacuum. After blending in the desired quantity of curing agent and repeated degassing the resulting resin can be spun on or cast against a substrate. Successively the applied layer has to be cured at room temperature over a minimum of 24 hours so that pre-expansion of microspheres can be avoided while cross-linking of PDMS matrix takes place.

It was found that the composite shows a maximum volume increase of about 270% at a bead concentration of 600mg/ml, whereas effect of mixing ratio of PDMS base and curing agent on expansion is negligible. For higher concentrations of microspheres however viscosity becomes to large counteracting the simple handling characteristics.

The composite can be both replica molded (Figure 2.6) with high fidelity through the use of a master form as well as applied to a surface via conventional spin-on process.

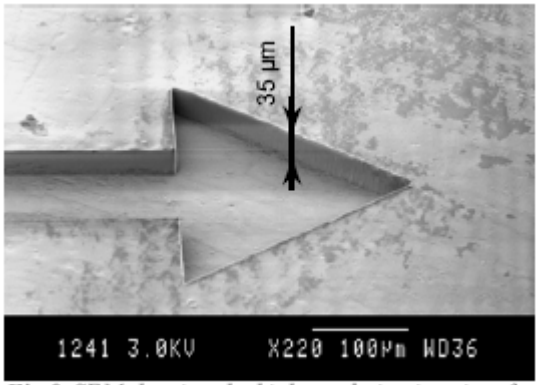

Figure 2.6: *SEM of a sample structure replica molded in the PDMS-XB composite (KTH-S3).*

In the latter case wafer level processing becomes possible and no special care needs to be taken to individually localize microspheres in the system. The form of the expansion can thus be individually defined by the form of an integrated heater located underneath the composite layer. A consecutive application of heat showed that a reservoir placed on top of the active layer can be filled out with very high resolution (Figure 2.7).

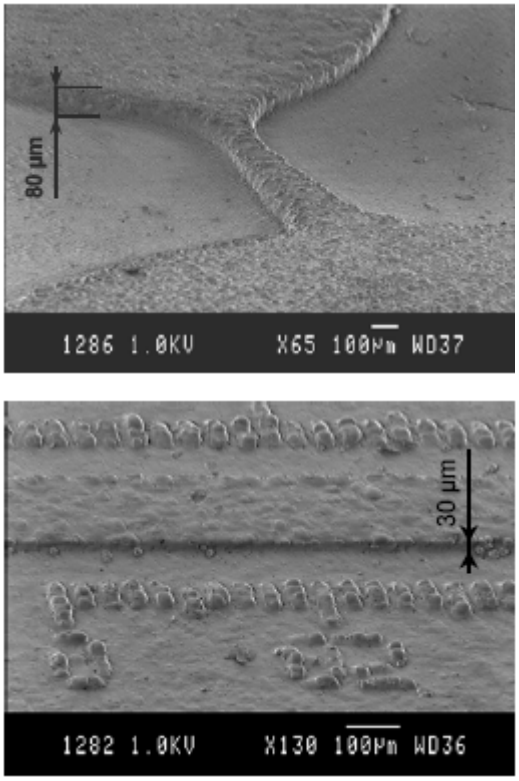

a)

b)

Figure 2.7: *SEM pictures of the microsphere composite after expansion into a) a 80mm deep polymer reservoir and b) a 30mm deep channel in silicon stacked on top of the composite layer (KTH-S3).*

Compared to pure expandable microspheres, the new composite shows similar outstanding volume expansion values and it retains the ability to hold the expanded form after switching off actuation heat. However more important, it adds significant ease to handling of beads, allowing for their adaption to highly integrated large volume, low-cost fabrication methods.

2.3.2 SINGLE-USE MICROFLUIDIC PUMPS AND VALVES

Based on this new composite material single-use pumps and valves for on-chip fluid control with high potential for integration into complex fluidic networks have been proposed in [19]. The design does not need external actuation or pressure sources since pumps and valves are actuated electrically with integrated heaters. Only low-cost materials and processes are used and the whole design therefor suitable for production of disposable devices. Figure 2.8 shows an outline of the multilayer structure constituting the device.

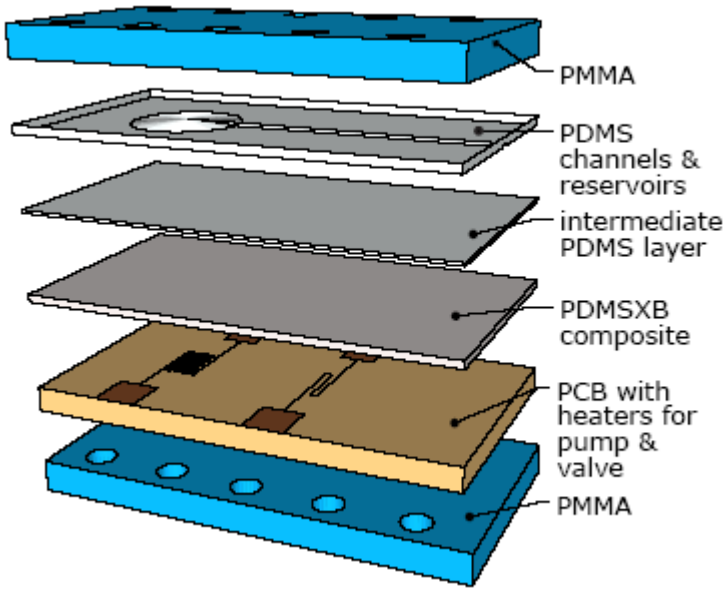

Figure 2.8: *Exploded view of device structure.*

Fabrication

A conventional printed circuit board contains the integrated heaters and serves as substrate for the polymer layers. The PCB is fully covered with composite actuator material PDMS-XB via spin-on technology. To guarantee isolation of fluid from the microbeads an additional thin intermediate layer of pure PDMS is applied as cover onto the composite layer via spin-on. A fourth layer of PDMS containing channels and reservoirs with common depth of 20μm is bonded to previous layers through oxidation in oxygen plasma. Prior to bonding, the fluidic channels and reservoirs are replica molded using a silicon wafer containing the inverse circular structures in a standard photoresist. The complete multilayer structure is then fixed between two PMMA plates providing both mechanical backing as well as fluidic access ports. Figure 2.9 shows a cross-sectional view of the inner layers of the fabricated device. The semi-circular footprint of the channel ensures complete sealing of channel by the valve. It is fabricated by a 200°C re-flow process applied to the resist patterns on the mold master wafer.

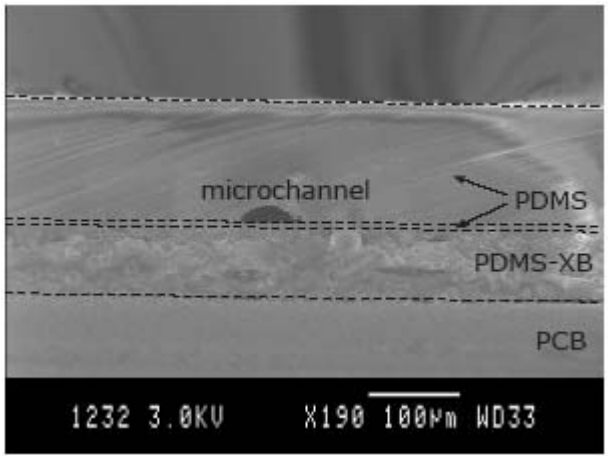

Figure 2.9: *SEM image of PDMS, PDMS-XB and PCB layer stack with microchannel in the middle (KTH-S3).*

Working principle

As depicted in Figure 2.10, a microengineered heater placed underneath the reservoir is needed to achieve controlled local expansion of the composite. This expansion leads to subsequent filling of the reservoir by the underlying layer which in turn expels a stored liquid outwards into a microchannel.

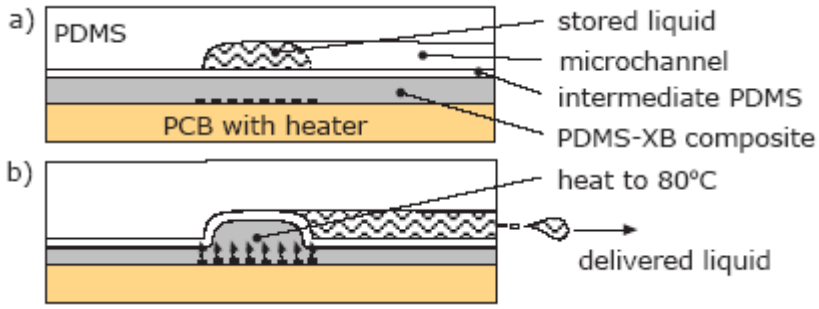

Figure 2.10: *Illustration of filled device a) and expulsion principle after application of heat via integrated heater b).*

For the valve structure the working principle is the same as for the pump with distinction that the expanded composite layer is used as an obstruction to block fluid flow through channel. An example of liquid dispensing from a reservoir is shown in Figure 2.11 for a mean heater power of 850mW applied over 3 seconds.

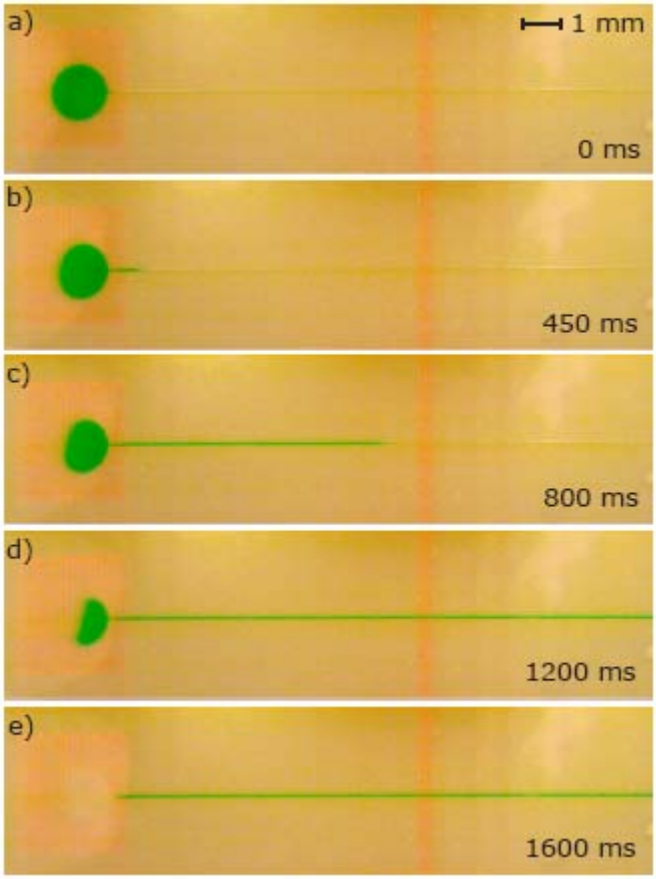

Figure 2.11: *Image sequence (a-e) showing 25nl of liquid being dispensed from reservoir (KTH-S3).*

Expulsion of fluid is possible against counter pressures of up to 100kPa with the time needed to dispense being highly dependent on the electrical power input. For valves it was found that they are able to withstand fluid pressures of up to 140kPa after being closed with 1W heater power applied for 8 seconds. Figure 2.12 shows valve operation in both open and closed state for a valve operated with 1W for 2.5 seconds. Maximum pressure at which leakage occurs is highly dependent on power applied to close the valve.

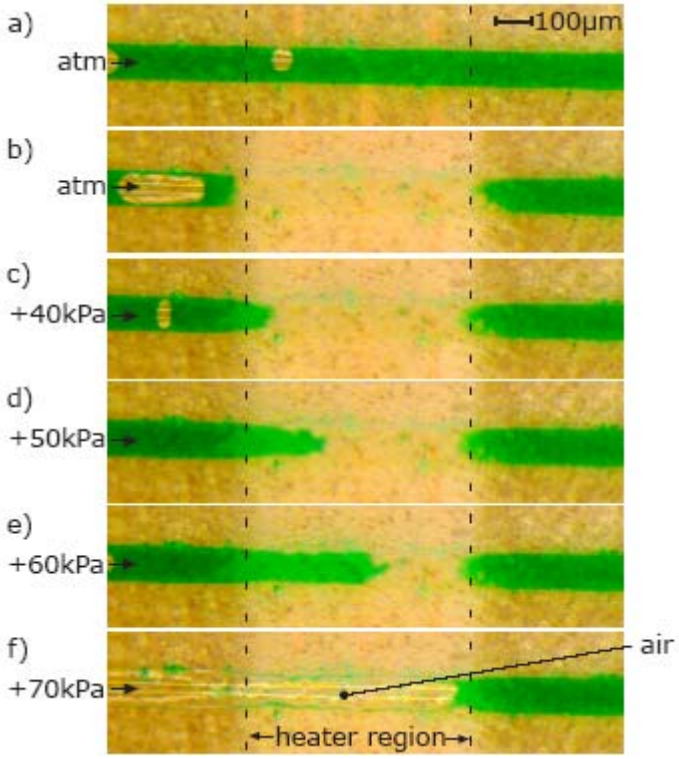

Figure 2.12: *Sequence of images showing valve operation for open state a) and closed state (b-e) up to breakthrough pressure f) (KTH-S3).*

2.4 SUMMARY

Expandable microspheres have been introduced as a novel actuator material for the handling of liquids. Whether as individually placed beads, mixed into a slurry or as composite, microspheres open up new ways of actuation for microfluidic applications. They are stable, low-cost, exhibit a relative large volume change, do not collapse after expansion and therefor do not need valve structures to prevent back flow when used in a pump device. In addition they also do not pose a packaging problem compared to other liquid or gaseous propellants. Most important however, in form of the new composite expandable microspheres allow for a very simple approach to the fabrication of highly integrated actuators for microfluidic systems. In summary these facts make them ideal for disposable portable biomedical applications as for example minimal invasive transdermal drug delivery devices.

Nevertheless, due to the thermal nature of actuation and especially in view of a potential commercialization in the medical field further research is needed. This thesis addresses two aspects fundamental to device optimization:

1. One imminent problem with the current design of composite based pumps is trapping of fluid in the pump reservoir during and after dispensing. Pumps for biomedical dosing applications demand exact control over the amount of fluid dispensed. Pumps presented here comply with this demand by defining the dosing amount through size of reservoir. However, as a result of the heat field produced by current heaters great care has to be taken regarding manual alignment of the layer containing microchannels onto the underlying layers. Since microsphere expansion begins at the hottest point it is essential to know the heat distribution over heater area to prevent parts of fluid being enclosed in the reservoir. Chapter 3 will address this by analyzing current heaters based on limitations of the fabrication procedure and design optimized heaters that will simplify manual placement of reservoir structures.
2. The second and most prominent problem arises out of the nature of actuation. Since a minimum temperature of approximately 70° C is necessary to start expansion of microspheres, an exposure of the fluid to temperatures exceeding safe operation parameters, as might be given for medical applications, must be avoided. For the success of microsphere-based devices it is therefore of utmost importance to be able to measure the temperature of the fluid in the reservoir and channel during operation. Chapter 4 will address this problem by employing a suitable measurement method to map the temperature inside the microfluidic system.

3 HEATER OPTIMIZATION

"Part of the inhumanity of the computer is that, once it is competently programmed and working smoothly, it is completely honest."
Isaac Asimov

Next to the composite itself, the most integral part of all devices based on expandable microspheres certainly is the actuator used to provide the heat needed for expansion of the microbeads. For the one-shot pump and valve, this actuator consists of a microheater fabricated in conventional printed circuit board technology [20].

Being a well established technology for production of electronic circuits, PCB technology is rather inexpensive compared to other MEMS fabrication methods like silicon processing. In addition, it allows for short time spans between design, fabrication and testing, making it well suited for prototyping purposes.

As a technology, printed circuits have found many applications in microfluidics, not only in interfacing fluidic and electronic components on one substrate [21], but also to directly integrate the microfluidic system into the copper layer [22]. Furthermore PCB technology has been proposed as a low-cost method to produce masters for the casting of polymer-based microfluidic systems [23,24].

In case of the device presented here, the technology is used to directly produce the heater structure (Figure 3.1) into the copper layer via standard printed circuit process steps. These steps include (among others)

1. creation of a photo-lithography mask,
2. application of photoresist to board
3. transfer of mask structures into the photoresist via exposure in UV-light,
4. development of resist,
5. etching of copper layer,
6. stripping of remaining photoresist.

The board with the heater then acts as a substrate for the functional layer containing expandable microspheres and bonded to that, the PDMS-based microfluidic system.

3.1 PROBLEM DESCRIPTION

Previous heaters were not optimized towards shape of the heat field they produce. As a consequence of the lack of spatial control over expansion of the microspheres, fluid can get trapped in the reservoir. Considering a heater as depicted in Figure 3.1, a constant trace spacing s and trace width w_{trace} lead to the highest temperature being located somewhere in the

middle of the meander shaped structure. This in turn causes expansion of the functional layer to begin in the middle of the reservoir, which often leads to some part of fluid being trapped in the rear end of the reservoir.

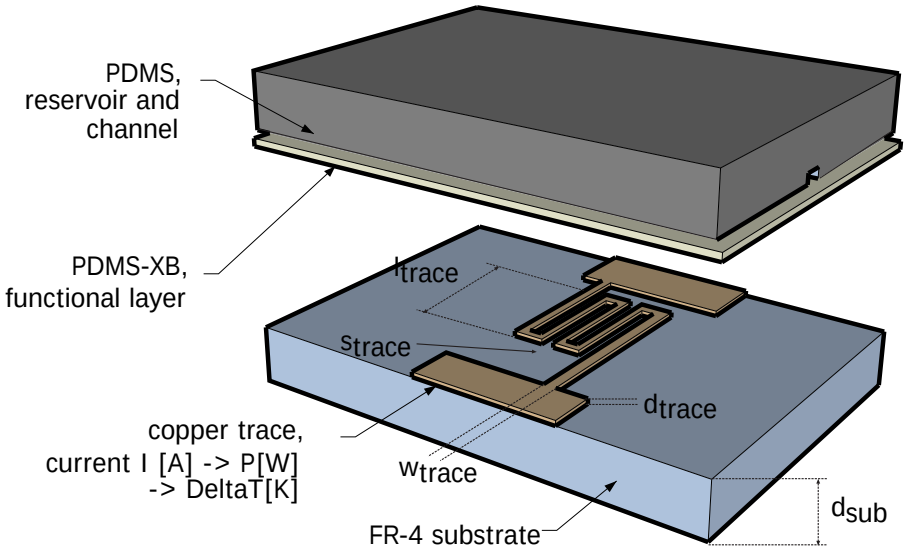

Figure 3.1: *Exploded schematic of device structure and parameters heater trace length, thickness, width and spacing, as well as substrate thickness (intermediate layer not shown).*

As a temporary solution to this problem placement of the channel system to heater can be adjusted in a somewhat trial-and-error like way. However, a smarter approach to this problem would be to design the shape of the heater in view of the corresponding heat field. In the following Finite Element Modelling (FEM) will be used to address this problem and find heater designs that allow for heat field distributions eliminating this problem. First the heaters will be analyzed to find available parameters and then optimized designs will be proposed with respect to limitations of the available fabrication process.

3.2 Physical Background

The temperature increase inside metal traces of the heaters is a result of the effect known as Joule heating, named after its discoverer James Joule. As with any conductor, an electrical current that flows through a copper trace on a PC board leads to a deposition of thermal energy into that trace [25]. The resulting temperature of the trace is then the thermal equilibrium between energy deposited by Joule heating on one side and cooling, due to convective and radiative losses via heat flux from the board to the surrounding environment, on the other side. When designing heaters on PCB with FR-4 as substrate material the maximum opera-

tion temperature should be well below the 110°C glass transition temperature for FR-4. This is the case for expandable microspheres where expansion starts at around 70°C.

3.2.1 MODELLING

The device in Figure 3.1 is modelled to consist of three material domains (copper for the heater, FR-4 for the substrate and PDMS as top layer) and two physical domains (the electrical and the thermal domain). Domain I is active in both physical domains with temperature dependence of resistivity and resistive heating as coupling variables.

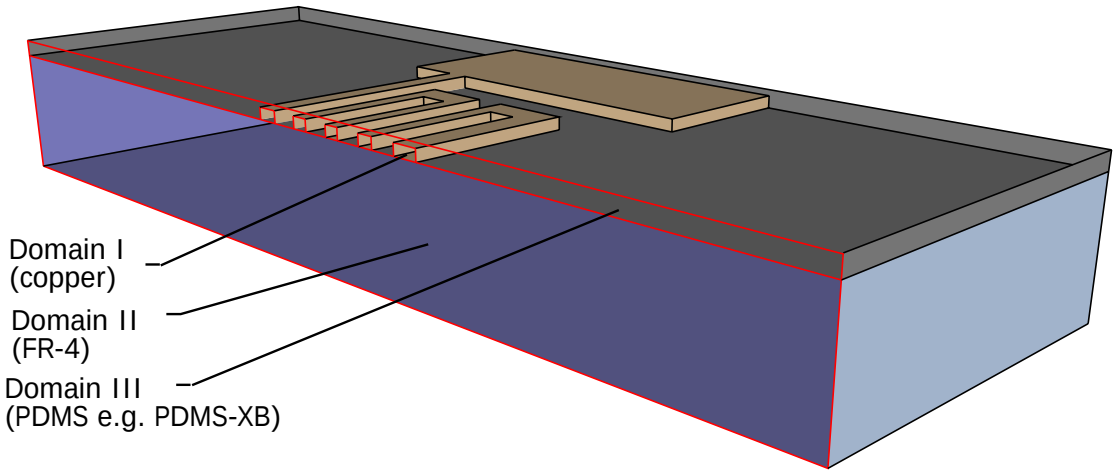

Figure 3.2: *Sectional cut depicting the three different material domains of the model.*

Domain II and III constitute dielectric materials and are therefore only active in the thermal domain.

Electrical Domain

The resistance of a trace on a FR-4 board can be described as follows

$$R_{el} = \frac{l_{trace} \cdot (1 + \alpha \cdot (T - T_{RT}))}{d_{trace} \cdot w_{trace}} \cdot \rho_{el}, \tag{3.1}$$

where R_{el} is the electrical resistance, l_{trace} the length of the trace, d_{trace} the thickness, w_{trace} the width, α the temperature coefficient of resistivity, T_{RT} room temperature, T the temperature and ρ_{el} the specific resistivity.

Using Ohm's law

$$U = R \cdot I \tag{3.2}$$

the power P [Watt] deposited into the trace as an effect of the current I [A] flowing through the trace can be written as

$$P = U \cdot I = R_{el} \cdot I^2 . \tag{3.3}$$

By rewriting Equation (3.2) with Kirchhoff's current law, which states that the sum of currents flowing towards that point is equal to the sum of currents flowing away from that point, the current balance in the trace becomes [27]

$$\nabla \cdot (-\sigma \cdot \nabla V) = 0 \tag{3.4}$$

with

$$\sigma = \frac{1}{\rho_{el} \cdot (1 + \alpha \cdot (T - T_{RT}))} . \tag{3.5}$$

For simulations, the boundary conditions used in the electrical domain are

$$(-\sigma \cdot \nabla V) \cdot n = 0 \tag{3.6}$$

for insulating boundaries with n being the unit vector,

$$(-\sigma \cdot \nabla V) \cdot n = j_0 \tag{3.7}$$

for the inlet of the current with j_0 being current density and

$$V = 0 \tag{3.8}$$

for ground.

Thermal Domain

The flux balances in the thermal domain are described by the heat transfer equations and coupled to the electrical domain by the term for thermal power generation density, $\sigma \cdot \|\nabla V\|^2$. In Equation (3.9) time dependence of the heat distribution is introduced as

$$\rho \cdot C_p \cdot \frac{\partial T}{\partial t} + \nabla(-k \cdot \nabla T) = \sigma \cdot \|\nabla V\|^2 , \tag{3.9}$$

where ρ is the density, C_p the specific heat capacity[1] and k the thermal conductivity. For electrically non-conductive materials this equation changes to

$$\rho \cdot C_p \cdot \frac{\partial T}{\partial t} + \nabla(-k \cdot \nabla T) = 0 . \tag{3.10}$$

While continuity of temperature is assumed for internal boundaries, the condition for boundaries with convective flux is described by

$$(-k \cdot \nabla T) \cdot n = h_{conv} \cdot (T - T_{inf}) + \sigma_{SB} \cdot \varepsilon_{em} \cdot (T_{inf} - T) \tag{3.11}$$

1. Heat capacity refers to the quantity that represents the amount of heat required to change one unit of mass of a substance by one degree. It has units of energy per mass per degree. This quantity is also called specific heat or specific heat capacity.

where h_{conv} is the convective heat transfer coefficient, σ_{SB}=5.67*10^{-8}Wm^{-2}K^{-4} the Stefan-Boltzmann constant and ϵ_{em} the surface emissitivity. At insulating boundaries conditions are obtained through

$$(-k \cdot \nabla T) \cdot n = 0 \tag{3.12}$$

and

$$T = T_{inf} \tag{3.13}$$

for boundaries with set temperature, where T_{inf} stands for ambient temperature.

Simplifications

In the following it will be assumed that thermal conductivity *k*, specific heat capacity C_p and temperature coefficient of resistivity α of the individual materials are temperature independent within range of interest. Since the thermal properties for PDMS-XB are not known and their measurement difficult due to the thermally induced expansion, microspheres in PDMS matrix will be approximated with values for pure PDMS.

3.2.2 PARAMETERS

As for the heater/substrate part of the device, trace width and length, trace spacing, trace thickness, as well as board thickness and board material, were identified as parameters with influence on the heat field distribution. Adjustments to all parameters are made in view of high power density and low overall power consumption.

Substrate

Darhuber et al. [26] have shown that for single trace heaters the achievable ΔT in relation to a heat sink at the bottom of the substrate increases with substrate thickness. An increase in ΔT is also found by Adams for plain single layer boards in comparison to double sided or multilayer boards and, on the material side, for polyimide[1] boards in comparison to FR-4 boards [25]. Due to availability of single-sided FR-4 boards with substrate thickness of d_{sub} = 0.5mm the corresponding parameters were fixed to these values in the work described here.

Heater

For the heater trace length l_{trace}, width w_{trace} and spacing s_{trace} as well as the thickness of copper layer d_{trace} are possible parameters. Since the copper layer on PCBs usually comes in standard thicknesses, the available d_{trace}=12μm was used. As can be seen from Equation (3.1) a small d_{trace} is desirable to reduce the power needed to reach a certain temperature. This is also true for w_{trace} and s_{trace}, however those two parameters are the ones with best accessibility and were therefore primarily modified.

1.Polyimide, thermal conductivity *k* = 0.3 W/mK.

3.3 SIMULATIONS

3.3.1 2D

To allow for short solution times and thereby enable fast adjustments to the geometry of traces in the heater meander the device was approximated by a 2D model as depicted in Figure 3.3. After definition of geometry, subdomain and boundary properties stationary heat fields as well as time-dependent temperature evolutions were calculated using the commercial FEM software Femlab version 3.0a (Comsol AB, Stockholm, Sweden).

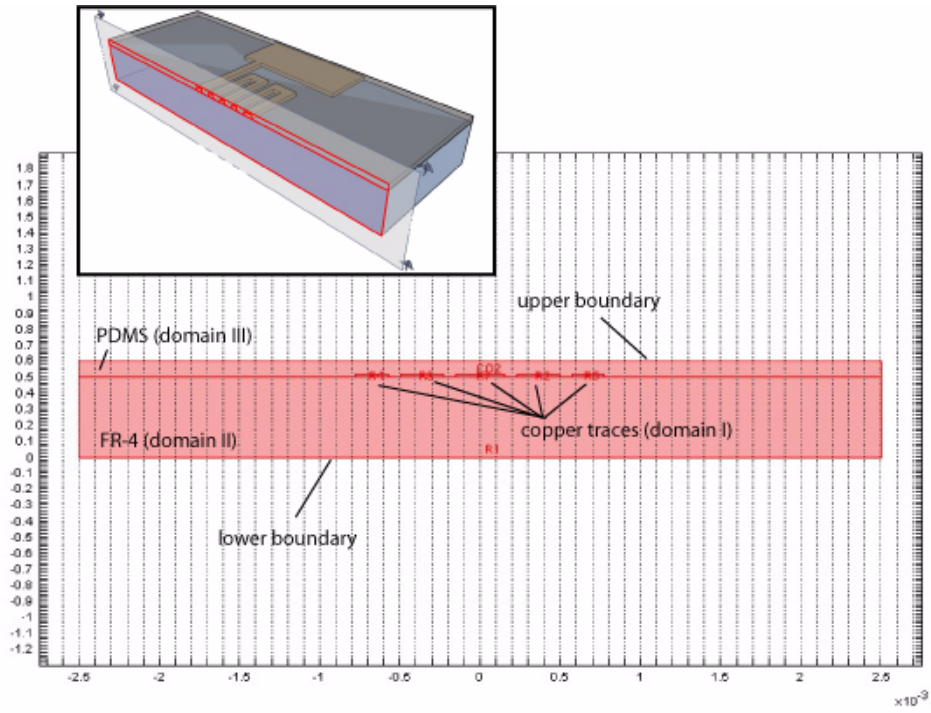

Figure 3.3: *Translation of the 3D device geometry (inset) into a 2D Femlab model.*

For all calculations the lower boundary of the substrate was set to room temperature and other boundaries to convective heat transfer plus radiation (Equation (3.11)) with T_{inf}=296K, h_{conv}=7.5 and ϵ_{em}=0.9. Table 3.1 shows material properties used in the subdomain settings and their respective sources. The power applied to the heater in form of a drive current was kept constant during simulations and introduced as a power density in the copper subdomains scaled according to the width w_{trace} of the individual trace. To display simulation results the temperature distribution along the upper boundary was plotted versus position. During simulations it could be seen that resulting stationary temperature distributions correspond to a linear superposition of solutions of individual sources, which was also mentioned by Darhuber et al.[26].

Material	ρ [kg/m^3]	c_p [J/kgK]	k [W/mK]	ρ_{el} [Ωm]	α	Ref.
Copper	8933	385	401	$1.72*10^{-8}$	0.0043	[20,29]
FR-4	1843	950	0.57 (x,y) 0.36 (z)	...	...	[28]
PDMS	0.97	1460	0.15	...	...	[30]
PMMA	1.19	1466	0.167	...	...	[29,30]

Table 3.1: *Material constants used in simulations. Entries denote density ρ, heat capacity c_p, thermal conductivity k, specific electrical resistivity ρ_{el} and temperature coefficient of electrical resistivity α.*

This fact was exploited by first simulating single trace heaters with equal power in Femlab, importing solutions into Matlab7 (TheMathWorks Inc.), interpolating and positioning the results according to their position in the actual heater, followed by summing and displaying the superposed curves. Temperature distributions produced this way correspond well with those of fully simulated heaters as long as the heater region was kept small compared to the overall model and could be used to estimate the shape of temperature distributions even faster.

3.3.2 3D

To complement the fast 2D heat-transfer simulations described above Femlab's abilities for solving fully coupled multiphysics problems were evaluated for a complete 3D model of a device. Convective heat-transfer mode and conductive media DC mode were coupled via the temperature-dependence of electrical conductivity (Equation (3.5)) and the internal variable for resistive heating, Q_dc. A valve type heater 2 consisting of material domains depicted in Figure 3.2 was constructed using Femlab drawing routines. As electrical input a constant current was applied to one external copper boundary of the heater meander while the other boundary was designated ground potential. In the heat transfer mode convective boundaries with equal values as in the 2D simulations were used for all but the underside which was set to room temperature. In Figure 3.4 the resulting temperature profile for this heater is shown after time-dependent simulation of a 3 second long constant current pulse.

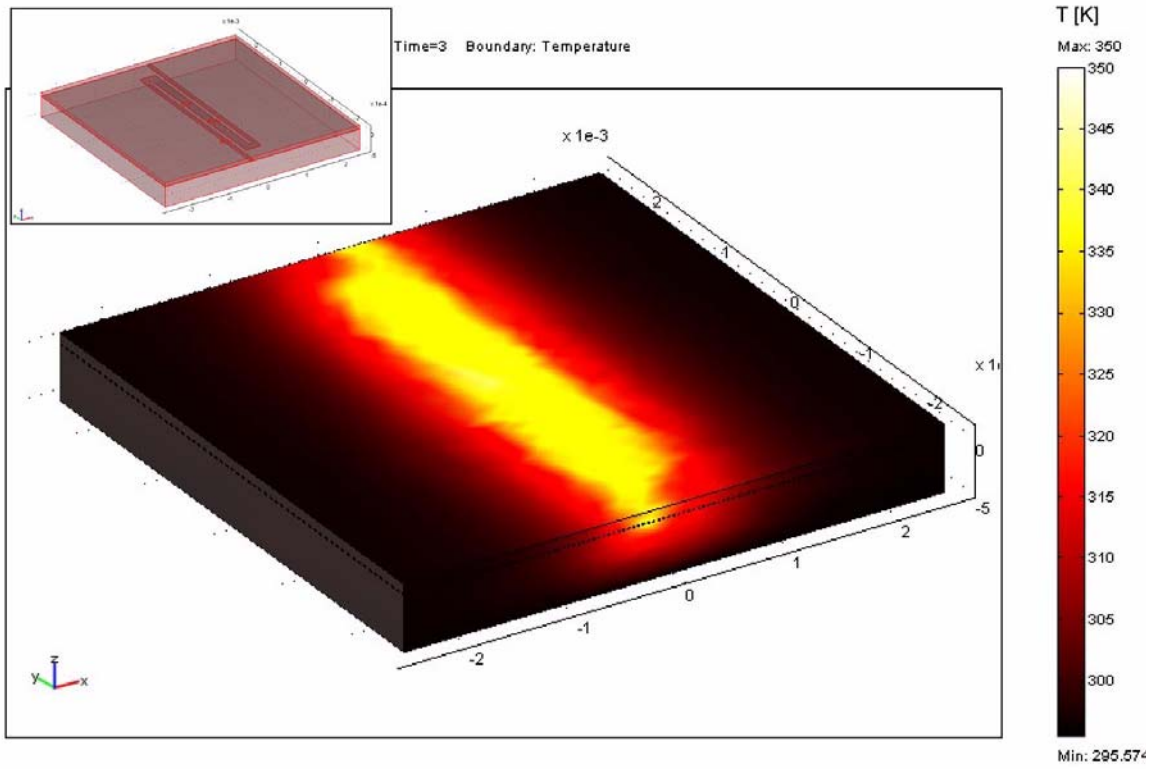

Figure 3.4: *3D simulation of temperature field of type 2 heater actuated with a constant current pulse I=1A for 3s. Inset: Femlab model of heater.*

It was found that, aside from a more cumbersome creation of the geometry in the Femlab interface, solution times in general increased significantly making instant heater shape adjustments impossible. Due to limitations of the current fabrication process for PCB and a large size of active heater area compared to reservoir footprint, the approximation via 2D model was found to be both sufficient and more flexible. However, for possible future designs where reservoir and heater are more equal in size, coupled-mode 3D simulations might become necessary to fine tune heater shape in the border areas.

3.4 DEVICE FABRICATION

The heaters designed above were used to fabricate two different devices, a “sharp” one with an active layer of PDMS-XB and a dummy device that would allow for steady-state heat field measurements to characterize heater design. In the latter case PDMS-XB was substituted with a layer of pure PDMS in similar thickness.

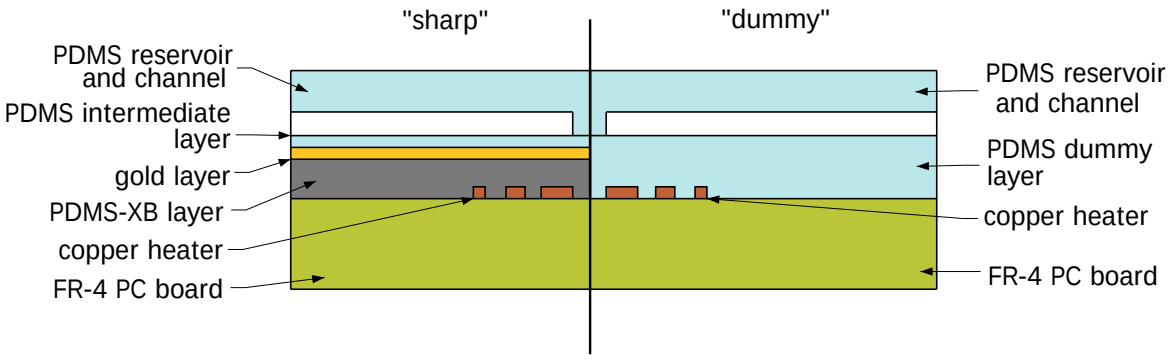

Figure 3.5: *Schematic of the two different device layouts fabricated. Left side: active device with PDMS-XB layer. Right side: dummy device with PDMS layer.*

3.4.1 HEATERS

Masks for the heater structures were drawn using L-Edit10 and converted to postscript file format via LinkCAD. They were then printed as negatives on high resolution photofilm by Valör Repro AB (Bromma, Sweden) with estimated minimum feature sizes of 25-30μm. PCB technology steps were performed in the department's printed circuit laboratory. As substrates 500μm thick FR-4 boards with a 12μm copper layer and negative photoresist film were used. Resolution limits of the PCB process were estimated to 100μm trace width and 75μm trace spacing.

3.4.2 POLYMER LAYERS

Functional layer

To fabricate the functional layer, portions of 4ml PDMS base (Sylgard 184, Dow Corning) were mixed with 1g of microspheres (820DU, Expancel) and degassed. Prior to application on the substrate 0.8ml of PDMS curing agent were added. The mixture was then spin-coated onto PC boards with typical speeds of 300rpm, resulting in an approximate layer thickness of ~100μm, and oven-cured for >60min at 50°C.

Gold layer

Due to reasons described in Section 4.3, a gold film in form of a thin decorative gold foil (Clas Ohlson, Insjön, Sweden) was manually applied to the top of the functional layer.

Intermediate layer

The uppermost layer in contact with the fluidic system was formed by spinning 4ml/0.4ml PDMS base/curing agent at 2000rpm onto the gold layer and curing it as described above.

For dummy devices only a PDMS layer was spun-on with a resulting thickness comparable to that of the combination of functional, gold and intermediate layer (ca 100μm).

3.4.3 CHANNELS

PDMS reservoirs and channels of various widths were produced by spin-coating an existing silicon master wafer containing up to 20μm high reflow-shaped photoresist structures with a mixture of 4ml PDMS base and 0.4ml curing agent at 250rpm. Subsequent curing was performed for 20min in an oven heated to 110°C.

Individual channels were cut out and carefully peeled off the master using removable adhesive tape as a carrier. To facilitate PDMS bonding, boards and channel surfaces were exposed to plasma for several seconds in a reactive ion etcher (RIE). After plasma treatment heaters and channels were manually aligned and brought into contact.

3.5 RESULTS AND DISCUSSION

The various heater shapes designed for this thesis are displayed in Appendix 6.1 together with their lateral dimensions, mask image and corresponding simulated 2D stationary temperature profile. Flat and sloped temperature profile heaters were designed using both fixed trace spacing/varying trace width and vice versa. The “circular” heater 4, mask1, was meant to provide additional in-plane focusing of the temperature profile but could not be tested since the etching step in the fabrication process could not resolve the geometric shape sufficiently enough.

Tests with fabricated flat profile heaters 1, 5, 6, 7, mask1 showed the same problems as previously used constant w_{trace}/constant s_{trace} heaters: expansion of PDMS-XB layer starts at a rather randomly distributed hot spot in the middle of the heater running outwards from there. This was mainly attributed to poor geometrical resolving of mask features during fabrication as observed via optical inspection, but also to some degree to limitations of the 2D model which does not take border effects at meander ends into account. As direct consequence of this mainly sloped temperature profile heaters will be considered in the following.

Varying width, fixed spacing heaters

As an example for this family of heater designs Figure 3.6 shows a sequence of images depicting the effect of the sloped temperature profile of a type 3 heater, mask2 on expansion of an overlaid PDMS-XB layer. The images were recorded using a firewire CCD camera attached to a microscope stage and a constant current I=1.5A was applied to the heater at t=0s

using a standard power source. It can be clearly observed how expansion starts at the lower end of the heater meander moving upwards until the active heater area is fully covered.

Although working in principle, these heaters were found to need significantly higher driving currents than comparable ones with constant w_{trace} simply due to wider traces. In addition they showed overheating and occasionally burned through at the thinnest traces. After optical inspection of the meanders, this was attributed to overetching in the PCB fabrication process and thereby poor translation of mask features into the copper structure.

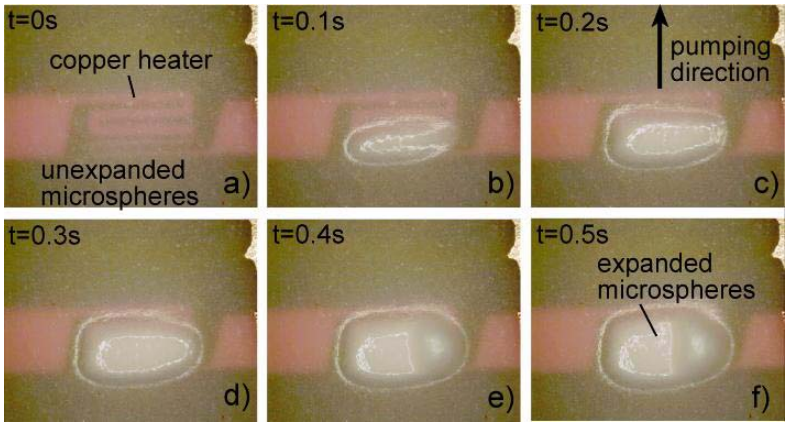

Figure 3.6: *Image sequence showing evolving expansion profile for a heater type 3 from mask 2. Note that for the images a piece of PDMS-XB composite was manually placed onto a bare heater and no top cover was used.*

Fixed width, varying spacing heaters

The best overall results in terms of evolving temperature profiles were found for heaters with constant w_{trace}=100μm and varying s_{trace}. This design variant exhibited an increased repeatability in fabrication compared to the combination of various trace widths in the same heater meander as described above. A second advantage of constant trace width proved to be lower driving currents necessary in comparison and thereby reduced risk for local hotspots at geometrical distortions.

Figure 3.7 shows an example of simulated time evolution of the temperature profile across a LabChip1 type heater. The shape of the profile was designed to support fluid delivery by gradually filling out a reservoir from left to right. It was successfully used in [31] to show nanoliter liquid handling in combination with performing a biological assay.

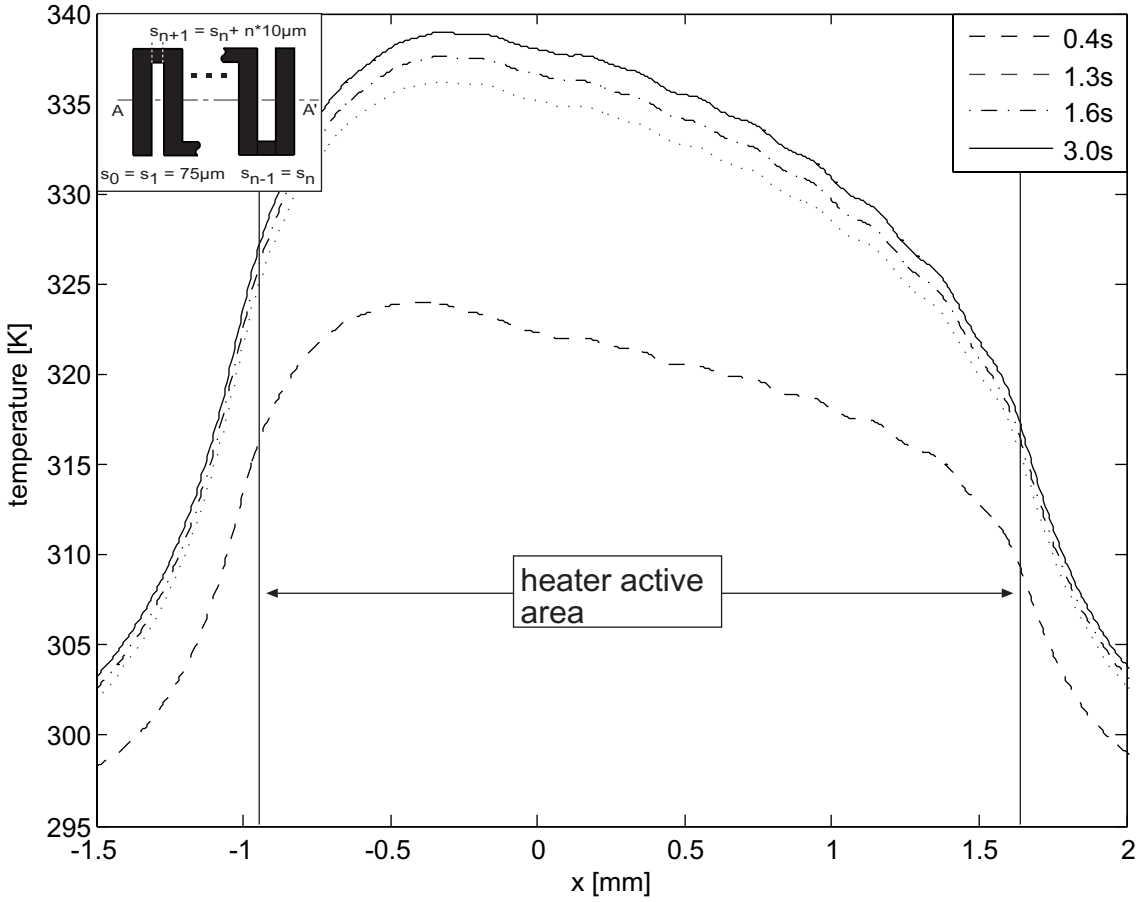

Figure 3.7: *Time-dependent simulation of temperature distribution across a LabChip1 heater. Driving current I=1A is switched on at t=0s. Inset in top-left corner shows the design rule for trace spacing of a type 4 heater, mask2, from which LabChip1 heater is derived by doubling the number of traces.*

Performance of the heater described above is shown in detail in Figure 3.8. At the beginning of the sequence small side reservoirs are filled and simultaneously emptied into the large middle reservoir using type 4 heaters. The mixture of the two liquids is then transferred further by use of a LabChip1 heater. Images a) to i) demonstrate the use of a sloped temperature profile to release mixture from reservoir without trapping parts of the fluid. The driving current is switched on for 2s beginning in a), expansion of PDMS-XB layer starts in the upper end of the heater c) and progresses continuously to full expansion which is reached in i).

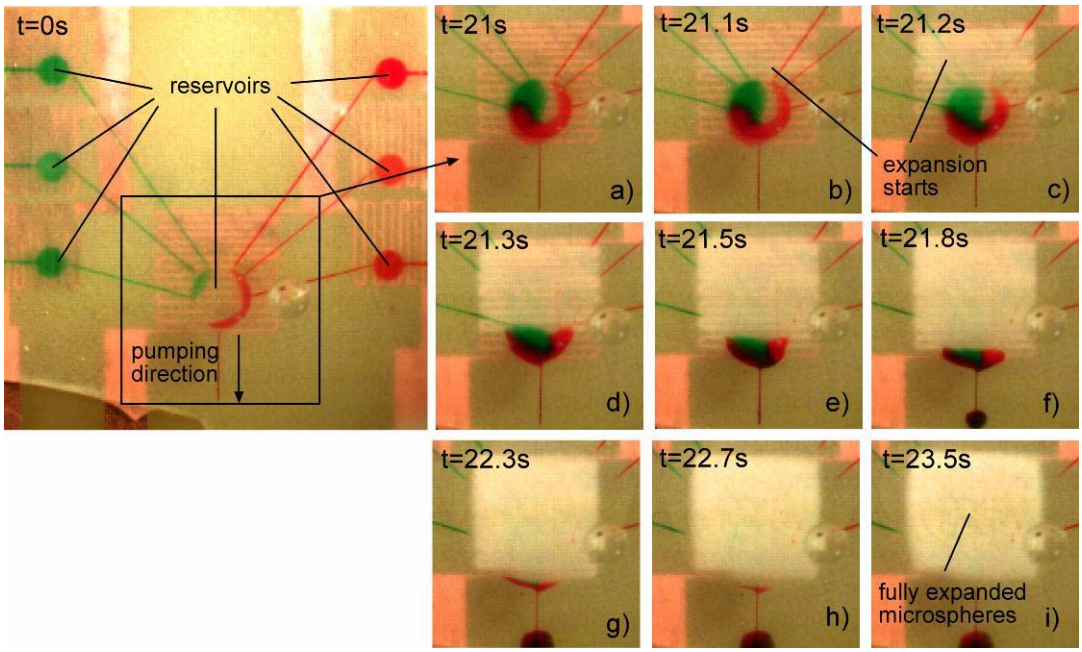

Figure 3.8: *Image sequence showing progressive localized expansion of PDMS-XB layer superimposed on a LabChip1 heater. Heating starts in a) and expansion evolves b)-i) in correspondence to the temperature distribution designed for this heater.*

In summary, it was shown how variations of trace width and spacing can be used to create custom shaped temperature profiles. While complying with the low-cost printed circuit fabrication process, demonstrated heaters provide controlled focusing in one dimension only. For future designs and further miniaturization of the microheaters additional control over the temperature profile especially in border areas of the meander could become desirable. This can be achieved by increasing the resistance in those regions where higher temperatures are required. However, since current heaters are already manufactured at the resolution limit of the available PCB fabrication process, this would require a change of technology which might make handling less straight forward and be a diversion from the low-cost approach.

4 TEMPERATURE MEASUREMENT

"Physicists like to think that all you have to do is say, these are the conditions, now what happens next?"
Richard Feynman

As mentioned before in Chapter 2, the thermal nature of the actuation principle used to expand the microsphere composite could potentially lead to an increase in temperature of the fluid to be delivered. For many substances especially in the biomedical field temperature limits exist. Exposure to values above this limit can eventually render a substance ineffective. To determine the applicability of this principle to certain types of fluids it is therefore very important to know the temperature a fluid will be exposed to during device operation.

Despite importance of controlled temperature distributions in microfluidic applications only few direct methods exist today to actually measure temperature in a microchannel or reservoir. One example discussed in [31] is to measure buffer temperature used in electrokinetic flow via changes in electrical conductivity. However, measuring average temperature, this process does not allow for spatial variations to be resolved. Other examples given like Nuclear magnetic resonance (NMR) or Raman spectroscopy either have similar resolution problems or offer only a limited acquisition rate.

The most promising methods currently in use employ the introduction of temperature sensitive probes such as nanocrystals, thermochromic colorants and liquid crystals or fluorescent dyes into the system. For thermochromic colorants thermal sensitivity is based on reversible color-change of microcapsule pigments when a certain temperature level is reached. By mixing several different pigments different ranges of temperatures can be covered. However, the main disadvantage of thermochromic pigments is that only transitions of certain temperature levels can be detected and that they are rather expensive. For nanocrystals and fluorescent dyes thermal sensing is possible due to the temperature dependence of quantum yield. Thermometry based on fluorescent dyes was chosen for this work because it allows for non-contact in-channel temperature measurements via use of a standard fluorescence microscope and commercially available fluorescent dyes.

4.1 FLUORESCENCE-BASED THERMOMETRY

4.1.1 INTRODUCTION

Historically, the method employed in this work and developed by Ross et al. [31] is an advancement based on what was demonstrated as Laser Induced Fluorescence or LIF for macro scale applications [37]. First used to measure concentration changes in chemical reactions

via concentration dependent intensity changes, LIF can also be used to measure temperature if molar absorptivity and concentration are kept constant.

The emission intensity of a solution containing fluorophores actuated by an appropriate source of illumination can be described as follows:

$$I_{FL} = I_{FL,0} \cdot A \cdot \phi \cdot \varepsilon \cdot L \cdot C, \tag{4.1}$$

where $I_{FL,0}$ is the excitation intensity, C the concentration of the fluorophore e.g. RhodamineB, ϵ the molar absorptivity, ϕ the quantum yield, A the fraction of the available light collected and L the sampling length along the incident beam. If all variables in Equation (4.1) except ϕ are kept constant the change of intensity of the reflected light can be used to measure temperature. This is possible since quantum yield ϕ of some fluorosphores like RhodamineB is highly dependent on temperature.

Ross et al. adopted this method to be used with a standard fluorescence microscope and CCD camera. Instead of a separate laser, the microscope lamp acts as light source in combination with a filter cube matching the fluorophore. Microscope optics determine spatial resolution and camera speed determines temporal resolution. Since the first publication on the method it has been used to measure effects of temperature gradient focusing [34], as well as Joule heating effects in electrokinetically driven microfluidic chips [35] and electroosmotic flow [36] respectively.

4.1.2 WORKING PRINCIPLE

Fluorescence-based thermometry builds upon the basic principle of standard fluorescence microscopy. A fluorescent dye is illuminated with an excitation wavelength range and, in return, emits in a range shifted relative to excitation wavelengths (Figure 4.2). Both wavelength regions are fitted to the absorption and emission spectra of the dye used and are defined by filters placed in the respective light path (Figure 4.1).

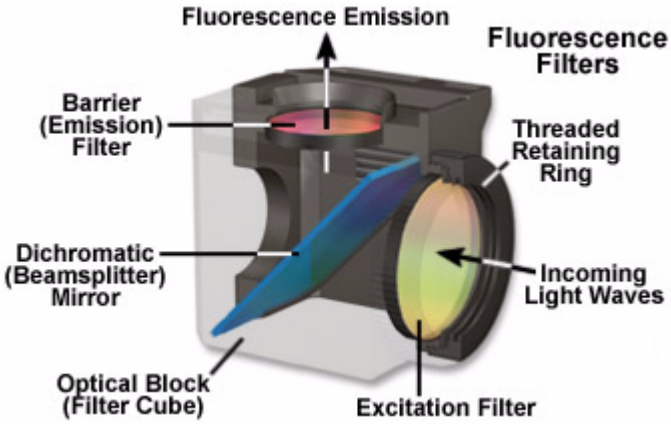

Figure 4.1: *Schematic of a filter cube used in standard fluorescence microscopy (www.microscopyu.com, Nikon)*

To measure temperature with this setup, fluorescence intensity of a diluted fluorophore solution at an unknown and potentially nonuniform temperature is compared to intensity at a known, uniform temperature. This is done by first recording a calibration curve for the relationship between relative change of intensity and temperature. Then the intensity of fluorescence of a fluorophore introduced into a microfluidic system is measured at room temperature and the temperatures of interest. Via calibration curve intensity changes can be translated into temperature values. Depending on the noise level and amount of averaging done, the accuracy of the temperature measurement was estimated by Ross et al. to be between 0.03°C for cross-channel profiles and 1.4°C for spatially resolved temperature distributions.

4.2 EXPERIMENTAL SECTION

Chemicals

RhodamineB was chosen as a fluorophore because its quantum yield shows a strong temperature dependence in the range of 0-100°C, with a relative change around 2%/K at 300K [38], which makes it ideal for use in aqueous systems. It was obtained as microscopy grade from VWR International (Karlskrona, Sweden). Buffer solutions containing 10mmol/L phosphate buffer at pH 7.4 were made by dissolving phosphate buffered saline or PBS (Sigma Diagnostics, St. Louis, USA) in 1L of deionized water. RhodamineB solutions of 100μmol/L were prepared by dissolving 12mg of RhodamineB in 0.25L of PBS buffer and subsequently stored at -20°C. Prior to use solutions were degassed and filtered using a 0.2μm Minisart™ syringe filter (Sartorius AG, Goettingen, Germany).

Image Acquisition

Fluorescence images of rhodamine dye were recorded using a Nikon ECLIPSE ME600 (Nikon Inc.) research fluorescence microscope. The microscope was equipped with a 2.5x (NA 0.075, working distance 8.8mm) and a 10x (NA 0.25, working distance 12.5mm) Nikon objective, as well as a 20x (NA 0.40) long working distance Olympus objective. As filter set, a TX Red Nikon filter cube with an excitation filter band of 540-580nm, a dichroic beam splitter at 595nm and an emission filter band of 600-660nm was available. Figure 4.2 shows the spectral profile for a Nikon Texas Red filter cube, where EX stands for excitation, EM for emission and Dichromatic Mirror describes the beam splitter between the two filters.

Using following approximation [39] for resolution R

$$R = 0.6 \cdot \frac{\lambda}{NA} \ , \tag{4.2}$$

and above values for wavelength λ and numerical aperture NA, the maximum achievable spatial resolution can be estimated to $R \approx 5\mu m$ for the 2.5x objective, to $R \approx 1.5\mu m$ for the 10x objective and to $R \approx 0.95\mu m$ for the 20x objective.

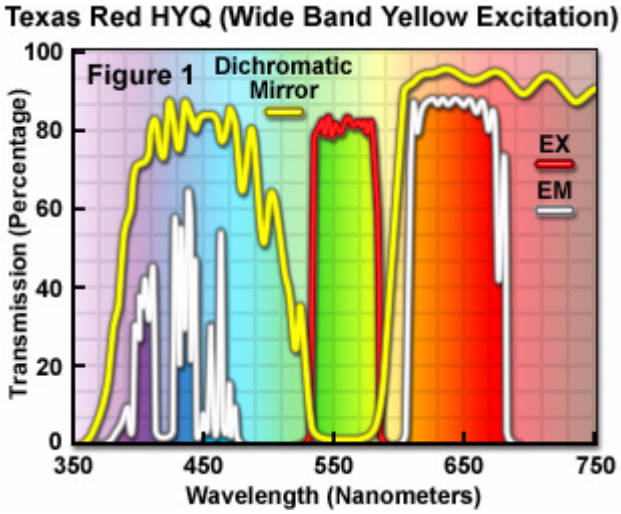

Figure 4.2: *Typical transmission spectral profile of a Nikon Texas Red HYQ filter set (www.microscopyu.com, Nikon)*

In the excitation light path three neutral density filters ND4, 8 and 16 could be added to reduce the intensity of excitation light and prevent photo-bleaching of the dye. Images were captured with a cooled Spot RT Monochrome CCD camera (Diagnostic Inc.) connected to a PC and controlled by Spot imaging software.

During imaging camera gain was kept constant at 1. Images were saved as uncompressed 16bit tiff files and analyzed using functions of the Image Processing Toolbox found in Matlab 7.

Calibration

To calibrate the temperature dependence of fluorescence intensity a T-shaped channel system was constructed in poly(methylmetacrylate) (PMMA) and mounted on a metal plate. A 50 Ohm power resistor was attached to the backside of the plate and used to adjust the temperature of the PMMA device using the metal plate as heat spreader. Reference temperature was measured by inserting a K-type thermocouple connected to a Fluke 8024 B Multimeter through the side port into the channel close to within 0.5mm of the imaging area. Fluidic access to channel was provided by two syringe adaptors. Figure 4.3 shows the mounted device with inserted thermocouple and sealed using silicone paste.

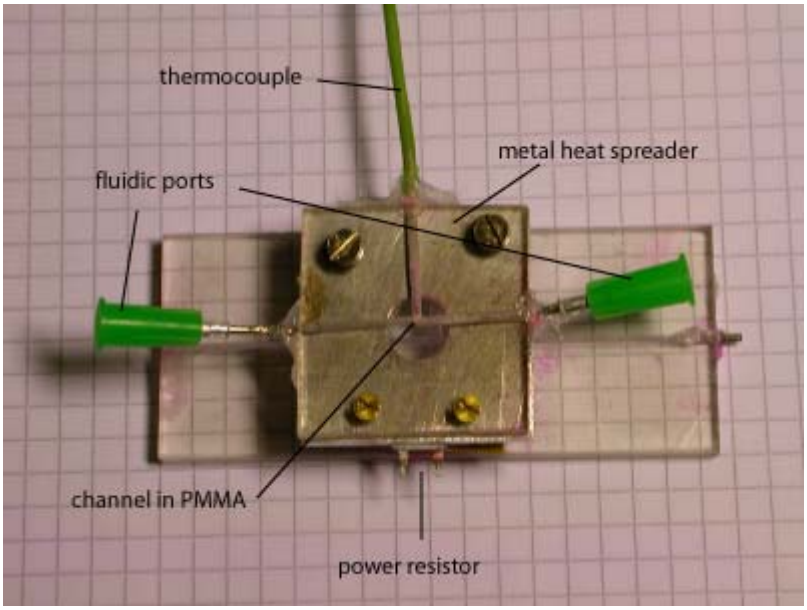

Figure 4.3: *Photograph of device used to record calibration curve for fluorescence-based thermometry.*

After filling the channel with RhodamineB solution a background image was recorded with excitation light shutter closed. Then a first picture was taken at room temperature using the 10x objective with excitation filters ND4 and ND8 inserted and camera settings as described above with an exposure time of 60ms. Following this, the temperature in channel was increased by increasing power to the resistor and the resulting fluorescence image was recorded at 5° intervals from room temperature up to 90°C.

Recorded fluorescence images were imported into Matlab7 via functions provided in the Image Processing Toolbox and their average intensity was measured for the corresponding temperature (see Appendix 6.3.1). Intensity values obtained were then normalized by intensity at room temperature and the temperature plotted as a function of intensity in the calibration curve shown in Figure 4.4.

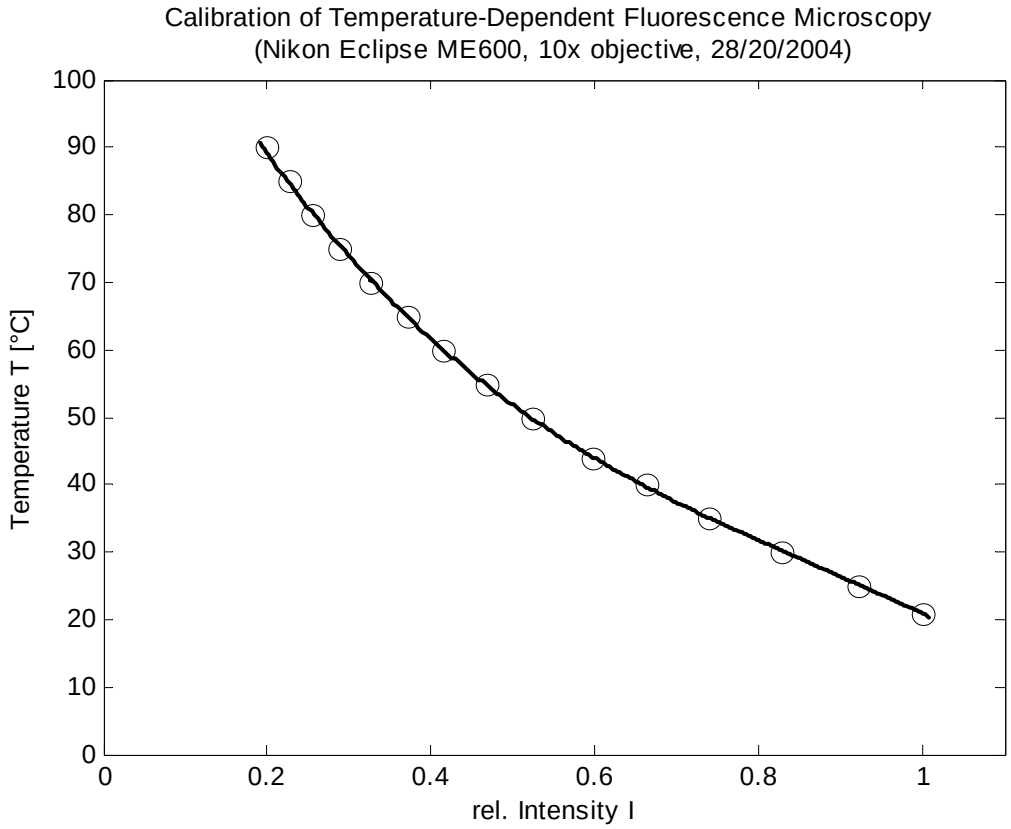

Figure 4.4: *Calibration curve used for fluorescence-based thermometry showing temperature as a function of normalized intensity.*

Open circles in the graph correspond to data measured, while the solid line is a third-order polynomial fit performed using the Matlab curve fitting tool to the data with following form

$$T = p_1 \cdot I^3 + p_2 \cdot I^2 + p_3 \cdot I^1 + p_4, \tag{4.3}$$

where T is temperature in °C, I intensity normalized to the value for 21°C and coefficients $p_1 = -85°C$ and $p_4 = 130°C$ fixed and $p_2 = (222 \pm 10)°C$, $p_3 = (-246 \pm 3)°C$.

This corresponds to Ross et al. [31] and shows that the calibration curve can also be applied for RhodamineB microscopy grade and buffer PBS pH 7.4 as used here.

A first calibration performed on a different setup using a L2001A fluorescence microscope (GX Microscopes, Haverhill, UK) and similar concentrations of RhodamineB dissolved in DI water only showed large deviation from the reported values (Figure 4.5). This was attributed to the influence of solvent and hence the resulting pH value [38] on quantum yield.

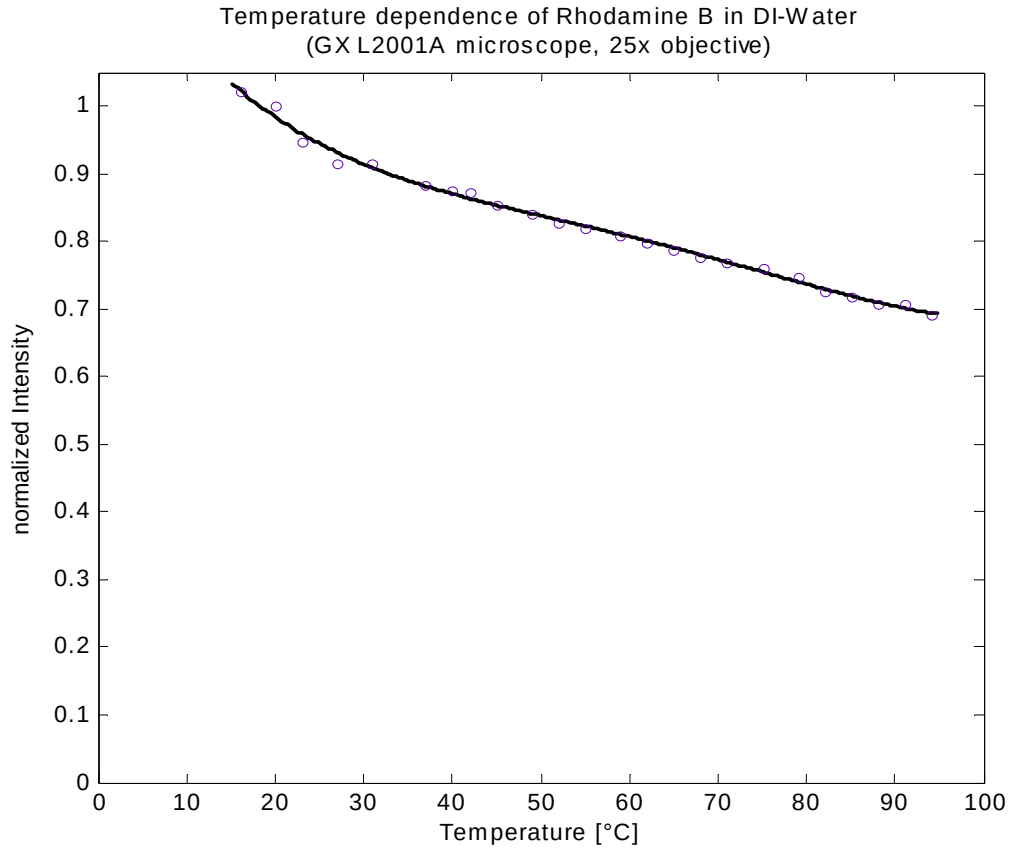

Figure 4.5: *Measured temperature-dependence of intensity for RhodamineB in deionized water. Open circles correspond to measurements, solid line is a fourth order polynomial fit. Measurement procedure as described above.*

4.3 HEATER CHARACTERIZATION

Fluorescence-based thermometry was first evaluated as a tool to characterize the heat field of heater designs described in Chapter 3. To be able to compare simulations to measurements the PDMS-XB layer in active devices was substituted with a pure PDMS layer on some heaters and a channel or reservoir were placed across the heater.

4.3.1 FILLING OF CHANNEL-STRUCTURE

Prior to measuring devices were filled with RhodamineB solution by cutting an opening into the channel under a microscope. A drop of filtered solution was placed onto the opening and the channel was evacuated through the drop by degassing the whole device in a vacuum container. Upon reopening of the container fluid is partly sucked into channel. To achieve further filling underpressure is applied to a second opening at the opposite side of the heater via a standard rotary air pump.

4.3.2 CHARACTERIZATION PROCEDURE

The heater was attached to a Switchbox SB60-5 power supply (Powerbox AB, Stockholm, Sweden) in constant current mode. Current and voltage were measured using standard multimeters. To begin measurement a background image with excitation light shutter closed and a reference image at room-temperature were recorded with no current applied to the heater. The current was then increased stepwise up to 1.2A with images taken at I = 0.3, 0.5, 0.8, 1, 1.1 and 1.2A.

Intensity change in recorded images was translated into temperature using the previously determined calibration curve specified in Equation (4.3). In Appendix 6.3.2 the developed image processing routine is shown as an implementation in Matlab code.

First the background is subtracted from all images and those with unknown temperature are divided through the one image taken at room temperature. For each image the temperature value at each pixel is then calculated using the calibration curve fit. After this images can be either displayed directly or temperature profiles can be created by averaging across the channel width.

4.3.3 RESULTS AND DISCUSSION

Figure 4.6 shows a series of false-color images of a microchannel superimposed to a type 6 heater recorded as described above. Individual images correspond to the steady state temperature distribution in the channel for driving currents from 0.3 to 1.2A. As can be seen in Figure 4.6, different temperatures were measured depending on the underlying material. Fluid on top of copper traces appears brighter (hotter) than in places covering substrate material FR-4. This phenomenon can also be observed in Figure 4.7. Here the gradient of temperature along the channel is displayed by averaging temperature across channel width. Depressions in the graph and outside the active heater area correspond to areas where the underlying substrate material is exposed.

To explain obtained results a cross-check measurement was carried out on the same device. This was done by placing a thermocouple on the device surface at locations along the channel length and measuring the temperature applying driving currents identical to those before. Results of this cross check showed that the actual temperature distribution along the channel corresponds to those values measured on top of pure copper.

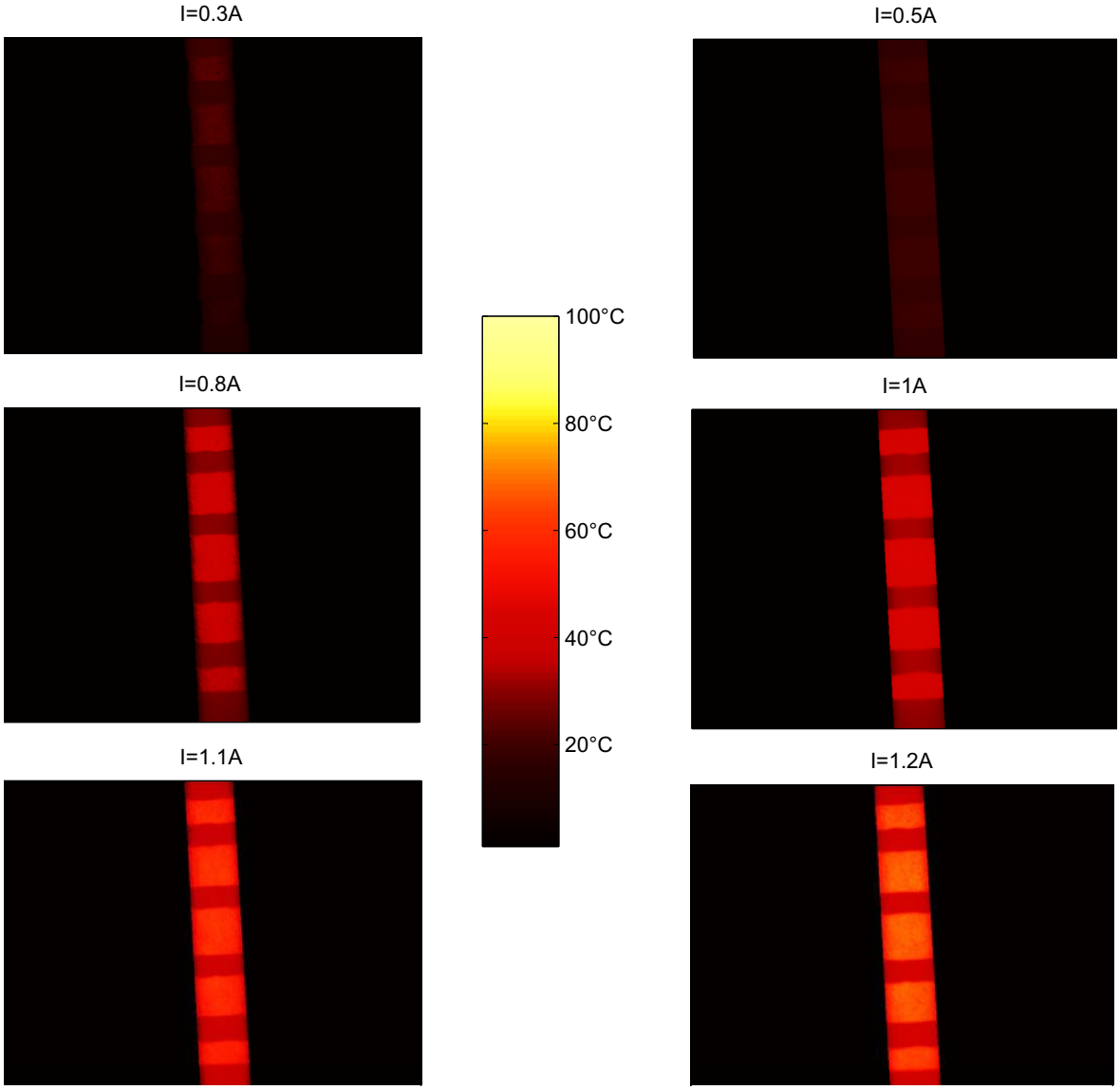

Figure 4.6: *False-color images showing steady-state temperature distribution in channel superimposed on heater 6, mask1 for currents from I=0.3 to 1.2A. Darker regions within channel correspond to areas with exposed FR-4, lighter areas to copper traces.*

Furthermore, observation of bare substrate material FR-4 under the fluorescence microscope showed significant emission in the wavelength region for emission as that of RhodamineB. It was therefore concluded that background fluorescence of FR-4 introduces an offset error in regions where substrate material is exposed. for fluorescence thermometry the relation between temperature and relative emitted intensity can be described as follows :

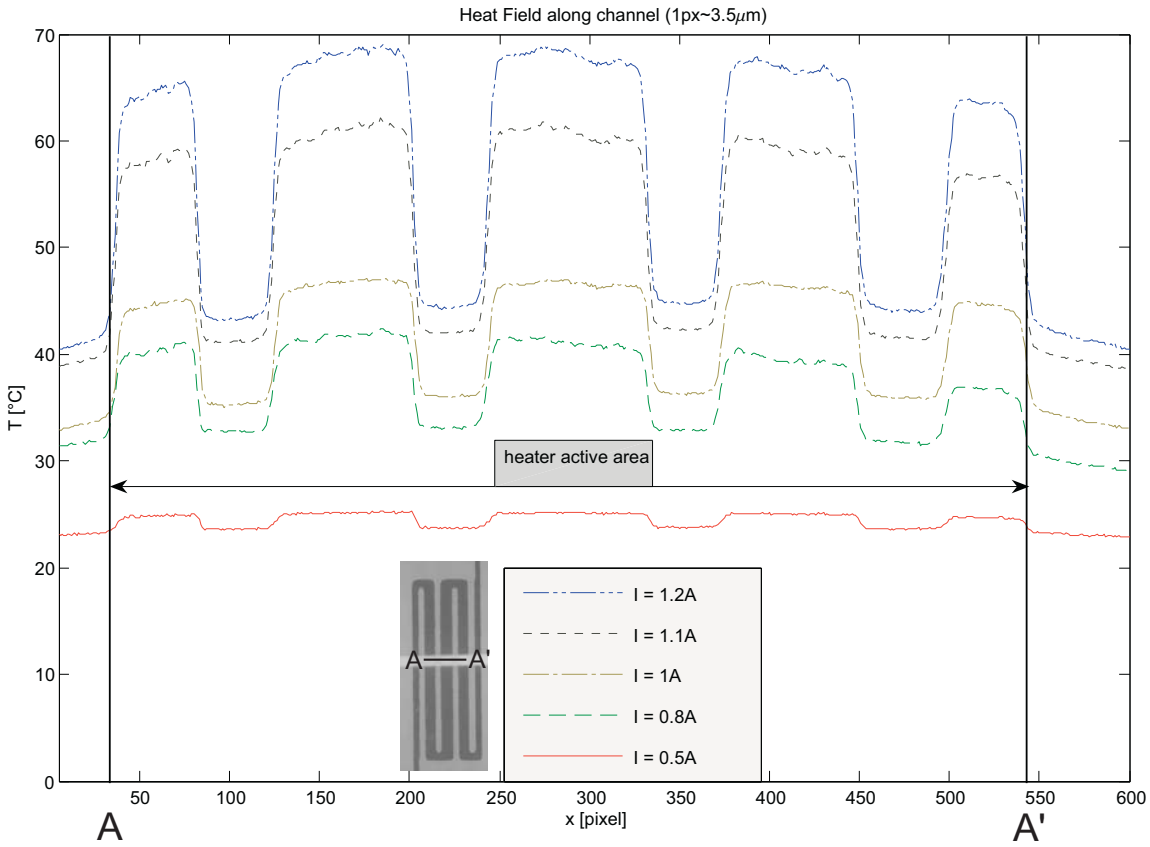

Figure 4.7: *Heat field over heater structure along AA' for different currents (heater 6, mask1). Inset: room temperature fluorescence image of channel and heater.*

$$T \sim \frac{I_T}{I_{RT}} = \frac{I_{T,RhB} + (I_{T,FR-4} = x)}{I_{RT,RhB} + (I_{RT,FR-4})}, \tag{4.4}$$

where I_T stands for intensity at an unknown temperature T, I_{RT} for that at room temperature and $_{\mathrm{RhB}}$ and $_{\mathrm{FR\text{-}4}}$ denote RhodamineB and FR-4 respectively. Combined with the fact that results are too low compared to those obtained by cross-check, one could deduce that the intensity change with temperature for FR-4 is smaller than for RhodamineB. For Figure 4.7 this would mean that in areas of FR-4 part of Equation (4.4) $I_{T,FR-4} = x$ decreases less with temperature than $I_{T,RhB}$ leading to a lower measured temperature as can be seen in form of indentations in the graph. However, as long as the exact temperature dependence of fluorescence for FR-4 is unknown, it is impossible to remove the offset via calculation.

As a result of this only data measured at location of the copper traces is put into account in Figure 4.8. The solid line in the graph shows the temperature distribution as simulated for a heater of the same dimensions using a 2D model described in Chapter 3. Comparison of

measurement and simulation show good agreement within the limits of measurement accuracy.

Since simulated data was obtained from a 2D model one would assume that temperatures measured on the device should be lower than those for the simulation. This assumption is due to the fact that in the model heat can only be dissipated by thermal conduction e.g. convection/radiation in z-axis (thickness of device), while in the real device heat losses also occur in-plane, such as for example through the copper traces.

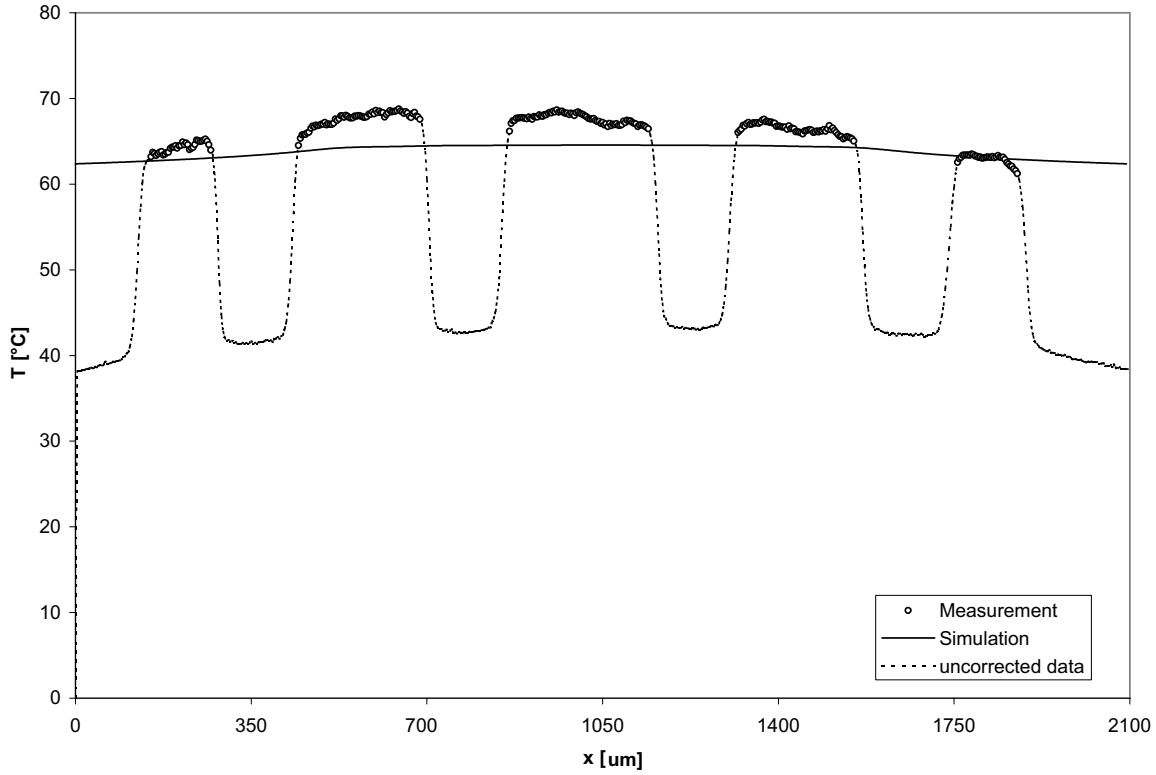

Figure 4.8: *Comparison of steady-state heat field distribution, measured (o) and simulation (-) for a current of 1.2A. Depressions in uncorrected data (---) correspond to offset error introduced by background fluorescence from FR-4 substrate.*

However, after optical inspection, the discrepancy was attributed to changes in the heater trace widths of 200μm and 275μm on mask, which translated into roughly ~150μm and ~250μm on PCB after etching. These smaller trace widths lead to increased resistance and thereby higher deposited power for a constant current, as can be seen from Equations (3.1-3.3).

4.4 TEMPERATURE MEASUREMENTS ON ACTIVE DEVICES

While the measurement method works well on the PDMS “dummy” devices, it proofed considerably more difficult to implement for active devices. One problem hereby turned out to

be the measurement principle itself. By comparing changes of intensity to determine temperature, other influences that also change the relative intensity ultimately lead to deviation in temperature measurement. This, for example, is the case in the reservoir on top of the heater as soon as the microsphere layer starts to expand. Fluorophore solution will be expelled from the reservoir and thereby decrease intensity. Reliable temperature measurements in the reservoir are therefore only possible until expansion begins or in the channel exiting the reservoir.

In addition, the problem of background fluorescence of FR4 in areas not covered by copper exists even for the PDMS-XB layer containing the microspheres. To use the copper layer as background by not etching it in areas underlying the channel leading away from the reservoir, was found not to be working. Microspheres in the PDMS-XB layer show as an underlying structure in fluorescence images taken and thereby complicate interpretation of the intensity change measurements. As a direct consequence different possibilities to enable the use of fluorescence thermometry in active devices were considered:

A first conclusion was to use a thin gold layer embedded between PDMS-XB and PDMS intermediate layer, which functions like the copper layer in dummy devices. The difficulty herein proofed to be the choice of a suitable deposition process for the metal layer. High energy processes could not be used because of temperature-dependent expansion characteristic to Expancel microspheres. Due to previous trials, it was opted to manually apply an ultra-thin gold foil as described in Section 3.4.

Whereas the gold layer applied accordingly allowed for successful application of the measurement method, the manual deposition led to problems such as an inhomogeneous background, channels blocked due to folds in the gold and a significantly decreased adhesion of polymer layers, which in turn made filling the channels very laborious.

As a second conclusion the reduced adhesion of the gold layer was used as sacrificial layer to mechanically remove PCB, PDMS-XB layer and gold from the backside. A conventional milling machine was used to remove almost the full thickness of the printed circuit board. Subsequently microsphere layer and gold layer were carefully cut away using a scalpel under a microscope. Resulting cavities were filled out with pure PDMS and cured at room temperature. Although this method cannot be used in the heater area, it proofed to facilitate measurement and interpretation of results in the channel areas by eliminating background artifacts.

4.4.1 METHOD

In principal the method used for measurements on the active devices is identical to what was described for the heater characterization in Section 4.3: fluorescence intensity images at known temperatures were compared to images taken at unknown temperatures.

To achieve this, the channel systems were filled by first cutting open fluidic ports at both ends, placing a drop of fluorophore solution on one opening and applying vacuum to the oth-

er opening using an air pump. After filling devices were clamped between two microscope slides and placed under the fluorescence microscope. The same powersupply as described above was used to manually apply a timed constant current pulse to the heaters. Prior to actuation a background image was recorded with closed excitation light shutter. The room temperature was measured and the camera set to record sequential images with typical exposure times between 60-300ms.

After 5 to 9 images were recorded at room temperature the current pulse was switched on for typically 2 to 3 seconds. Images were then processed using Matlab by subtracting the background image, dividing through the image at room temperature and translating the intensity change into temperature via the previously recorded calibration curve. Appendix 6.2.3 shows an example of the Matlab code used including the subroutine to do averaging over channel width.

During imaging it could be observed that the risk for photo bleaching to occur over the complete image sequence increased significantly when no neutral density filters were introduced into the excitation light path. This can lead to a reduction in intensity of the fluorescence signal and thereby higher measured temperature values. No effect was observed when using filter ND4. However, reduced fluorescence emission signals require increased exposure times and thus make it more difficult to record the fast expansion process.

4.4.2 RESULTS AND DISCUSSION

Current pulse on dummy device

To estimate the temperature increase in a reservoir on an active device equal driving currents were first applied to a dummy device where the PDMS-XB layer was exchanged with pure PDMS. All images were recorded using a 2.5x objective with an individual exposure time of 0.15s.

The upper part of Figure 4.9 shows a room temperature fluorescence image of a 200μm wide channel filled with RhodamineB solution on a type 6, mask1 heater. Since no intermediate gold layer was used in this device, the heater structure beneath can clearly be distinguished from the fluorescent PCB material. In the lower part of Figure 4.9 a sequence of images shows the decrease of fluorescence intensity as a direct consequence of temperature increase from room temperature in the channel due to a constant current pulse (I = 1.15A, t = 2.94s) applied at sequence number 0010.

This intensity change is translated into temperature values for areas with copper underneath as described above. Figure 4.10 shows the measured temperature profile along length of a channel as obtained by averaging across channel width. Values for areas between the heater meander correspond to a linear interpolation. Time lapse from one sequential image number to the next is 1s for all measurements. This is due to the camera system used which only allowed images to be recorded at a framerate of 1Hz.

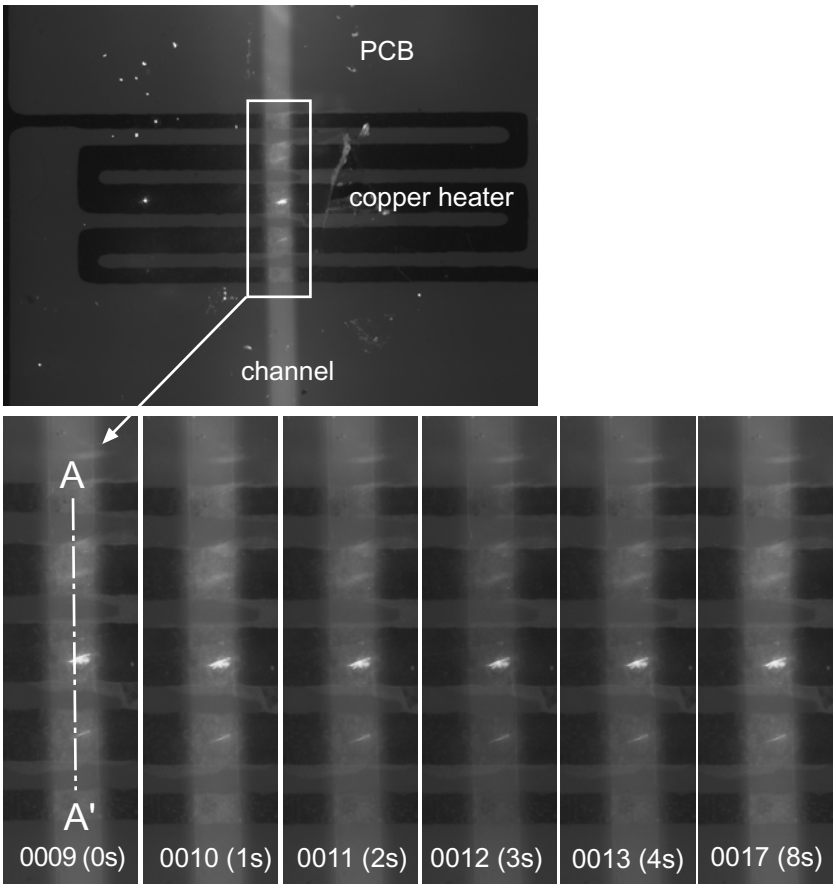

Figure 4.9: *Fluorescence image sequence of channel filled with RhodamineB solution on type 6, mask1 heater. Constant current pulse I=1.15A is switched on at image 0010 for 2.94s. Changes in intensity from 0010 to 0017 are due to the temperature increase in channel and cooling down subsequently.*

As expected, the shape of the temperature profile corresponds to meander geometry. The thinnest traces at the edges account for the highest temperature change in the fluid-filled channel (curves 0011, 0012). Furthermore, after switching of the current pulse, temperature decreases fastest in direction of channel outlets (curves 0013, 0014, 0017) represented by the temperature maximum shifting into the middle of the heater. This is a result of different thermal conductivities of fluid and surrounding polymer walls. The RhodamineB solution used has a thermal conductivity of 0.6 W/mK, about four times higher compared to PDMS (0.15 W/mK). PDMS therefore works as thermal insulation except for in direction of the channel.

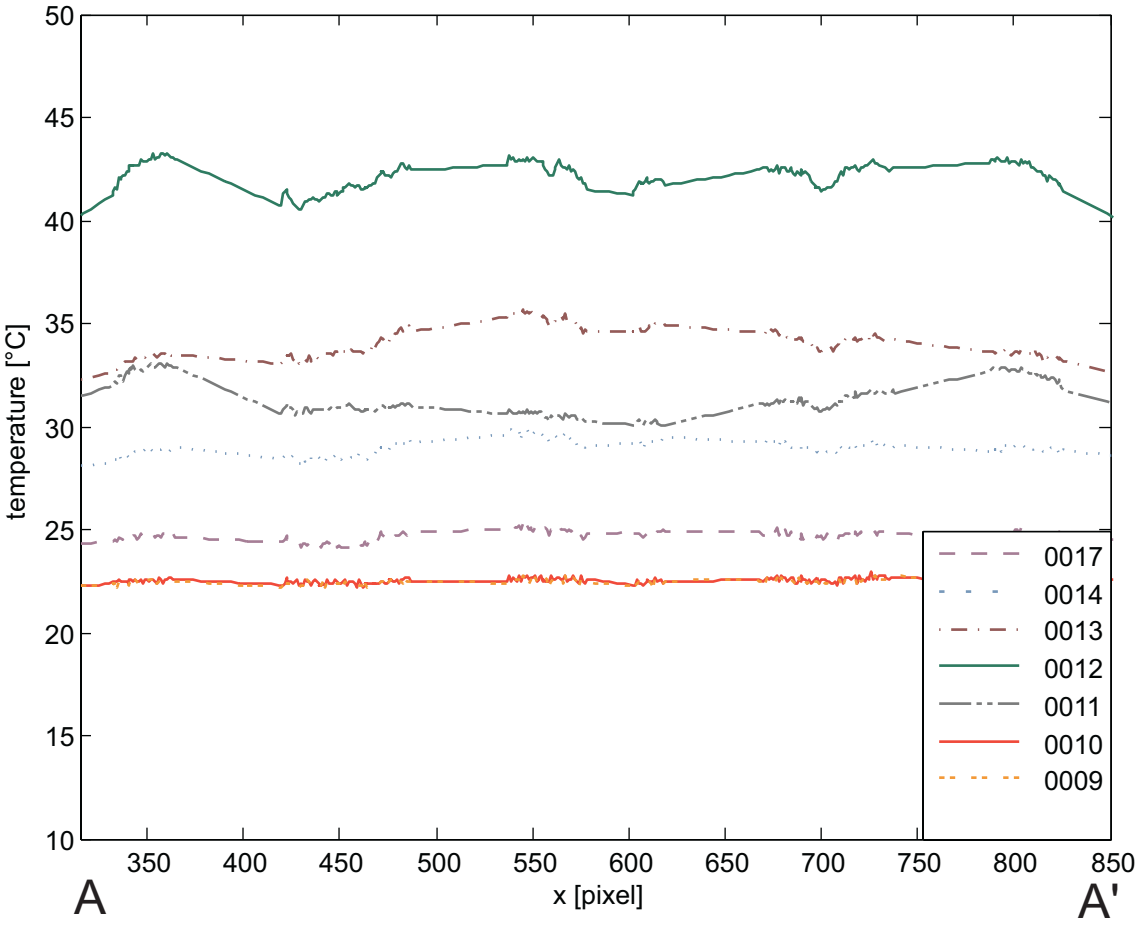

Figure 4.10: *Temperature distribution in channel across type 6 heater along line AA'. Current pulse I= 1.15A (2.94s) is switched on at 0010. (1 pixel ~3.5μm).*

Using results of measurements described above, Figure 4.11 compares peak temperature in the channel as a function of sequence image of two different pulse currents. For both curves the pulse is switched on at image 0010, with the current being 1.15A (~0.8W, 2.94s) for blue and 1.55A (~0.8W, 3.35s) for black curve. While the latter leads to a measured peak temperature of 67.6°C, the maximum temperature for the lower current peaks at 43°C. Concluding from these results we assume, that the fluid temperature in active devices ranges well below 43°C. This assumption is supported by the fact that typical actuation pulses for active devices compare to <1.15A and <=2s [19,31] and that part of the thermal energy is translated into phase-change and consecutive expansion of microspheres in the PDMS-XB layer.

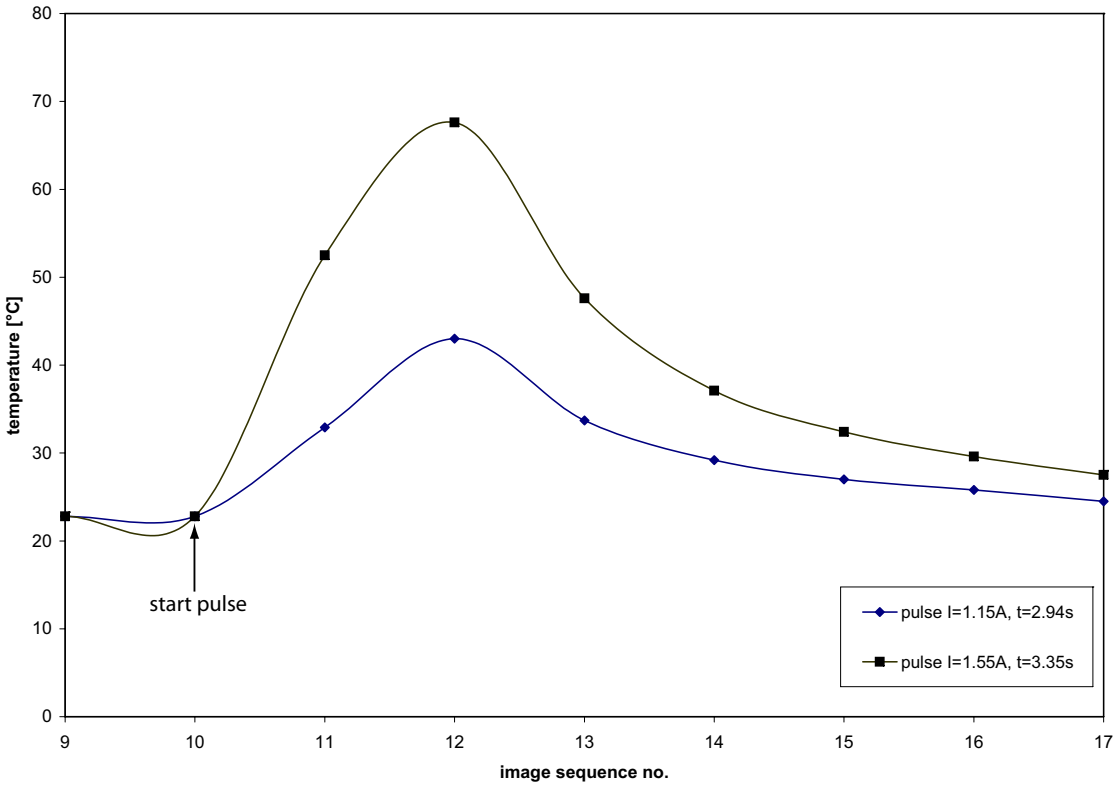

Figure 4.11: *Peak temperature in channel for two different drive pulses. Current is switched on at image number 10, with time-spacing between images of 1s.*

Current pulse on active devices - gold layer

In Figure 4.12 the measured temperature profile in a channel at the reservoir outlet for a current of I=1A (3.12s) is displayed. The device consists of a gold layer separating a type2, mask2 heater and the fluidic part with a channel width of 100μm in PDMS. A fluorescence image depicting the device is shown as an inset. Pumping occurs in direction of arrow and temperature values are averaged over the channel width along the line A-A'. As mentioned before, temperature measurements in the expanding area cannot be translated (into temperature values) for images recorded after the expansion started. This is the case for curves 0011-0018 for pixel 0 to 300 where expansion of the microsphere composite can be observed in the corresponding fluorescence images. In the channel to the right temperature increases to a maximum of 32°C between 3-4s after the current is switched on at sequential image number 0010. After switching of the power the temperature decreases in the channel direction, indicating heat conduction in the fluid.

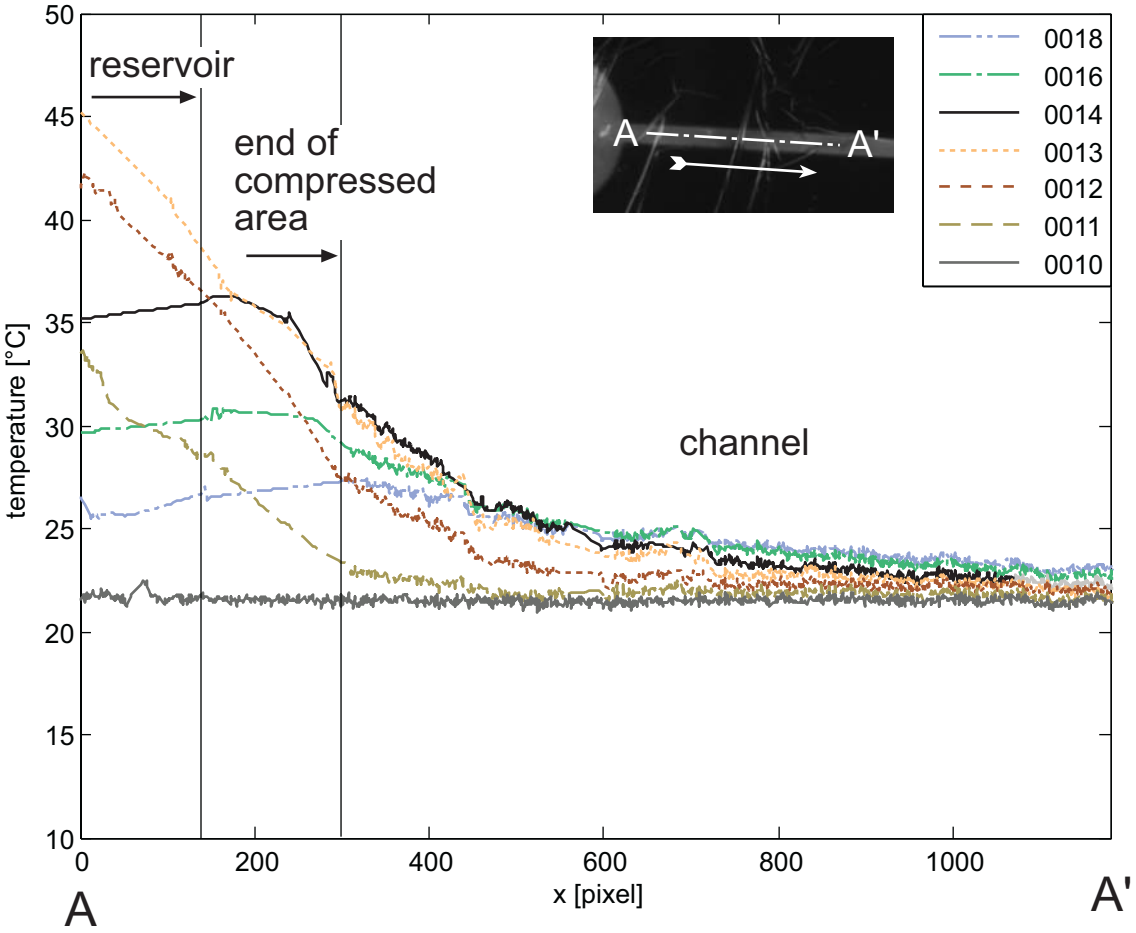

Figure 4.12: *Temperature profile along line AA' on gold device (heater type2 mask2). Current I=1A is switched on for 3.12s at image sequence number 0010. Temperature is averaged over width of channel. Inset: corresponding fluorescence image 0010, arrow depicts pumping direction (1 pixel ~3.5μm).*

A further example of devices using the intermediate gold layer is shown in Figure 4.13. Here evolution of the temperature profile is given for the horizontal part (x-axis) of a channel 400μm downstream from one of the reservoirs on a LOC system (see [31]), similar to that displayed on title page. For actuation a current pulse of I=1.2A (3.37s) is applied to a LabChip1 heater starting at 0010. Again, location of measurement and pumping direction are displayed as inset via a fluorescence image of the channel corresponding to sequence number 0012. About 2 seconds after the current is switched on a maximum temperature of close to 35°C is measured. This is slightly higher then for the example above especially considering the additional distance to the reservoir. While the increase in current might be an explanation, it also has to be taken into account that graphs for measurements performed on gold (as a result of the usually rather inhomogenous background) in general contained more noise compared to those on a PDMS window.

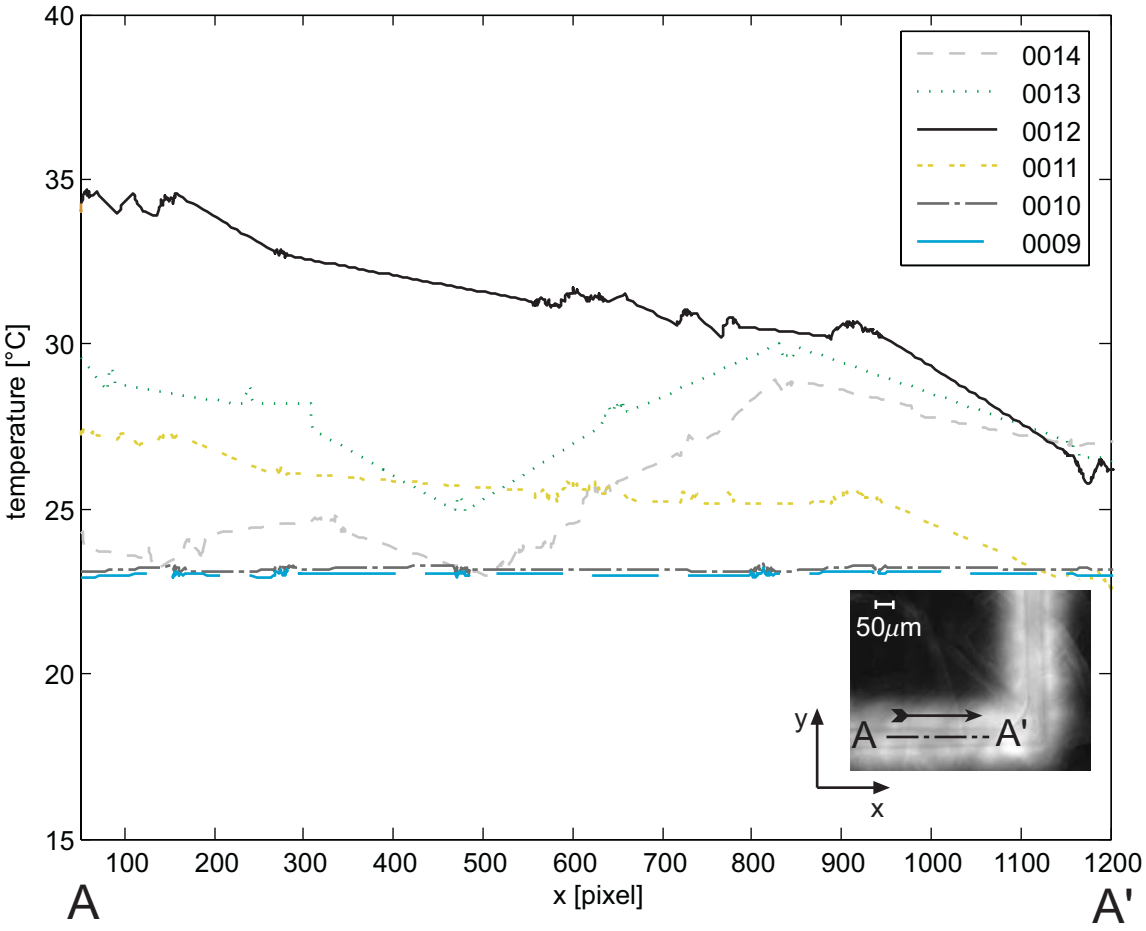

Figure 4.13: *Temperature profile averaged across channel width along AA' on gold device (LabChip1 heater). Pixel 0 is located 500 μm from the reservoir outlet. Current I=1.2A (3.37s) switched on at 0010. Inset: fluorescence image of channel, arrow depicts pumping direction. (1 pixel ~0.35μm)*

Current pulse on active devices - PDMS window

In comparison to the gold devices discussed before Figure 4.14 shows the temperature profile in a channel of equal width on a LOC system with 50μm wide channels. For this example the channel is located on a PDMS "window" machined into the PCB. A current of I=1.15A is applied for 2.25s to a LabChip1 heater underneath a reservoir located 500μm upstream of pixel 100. After actuation starts at graph 0010, warmer fluid from the reservoir is approaching the channel section in 0011. The temperature increases further until graph 0012 and transportation of fluid stops at 0013 with a maximum temperature in the channel section of 31°C. No more heating occurs after power to the heater is disconnected and the temperature profile begins to level out via heat conduction (graph 0014 to 0018).

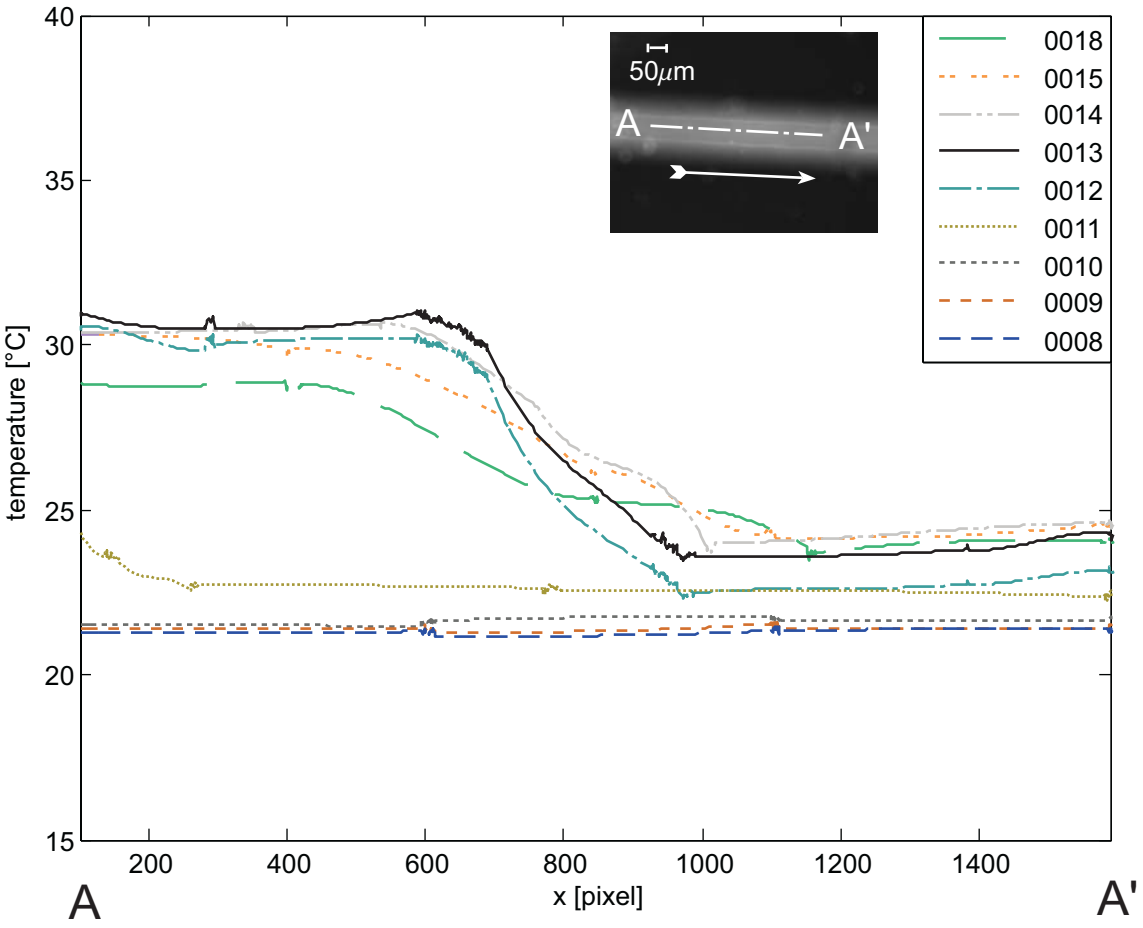

Figure 4.14: *Temperature profile in channel on PDMS window (LabChip1 heater) for current I=1.15A (2.25s) starting image 0010. Inset: fluorescence image of channel with pumping direction. (1 pixel ~0.35μm)*

In summary, data collected for changes of the fluid temperature as result of the actuation principle indicates peak temperatures up to 35°C. This is well below the 70°C necessary to start microsphere expansion in the composite. Furthermore, it corresponds with results in [31], where a biological assay with reduced thermostability of below 39°C was successfully performed following transportation via similar pumps as described and characterized in this report.

5 CONCLUSIONS

"Nothing shocks me. I'm a scientist."
Harrison Ford, as Indiana Jones

Two problems fundamental to fluidic devices based on the novel thermally activated microsphere composite were addressed in this report.

Partial fluid enclosures in the pump reservoir were responded to by specially designed temperature profiles. Various temperature profiles were developed by simulating variations in width and spacing of micro heater traces. Resulting heater designs were fabricated in printed circuit board technology and their effect on time-based progression of the composite expansion evaluated. Additionally fluorescence based thermometry was adapted to measure and compare temperature profiles of fabricated heaters corresponding to simulation results. Finally, designed heaters were employed on a low cost disposable lab-on-a-chip system and their shaped profile was used to demonstrate nanoliter liquid handling [31].

As a second problem potential heating of transported liquid was investigated. Temperature changes in fluid-filled systems were measured during actuation. For this purpose fluorescence based thermometry with RhodamineB as fluorophore was calibrated and used to directly measure fluid temperatures. A PDMS based dummy device was developed to measure and estimate the effect of typical actuation currents on fluid temperature change. Active composite based devices were modified by introducing an intermediate gold layer to facilitate measurements. Furthermore, this gold layer was used as a sacrificial layer to fabricate devices with PDMS observation windows. Measurements on dummy devices indicate a temporary fluid temperature increase up to 40°C. Active devices show peak temperatures up to 35°C. While recorded temperatures can be used to determine if the delivery device presented is applicable to a certain substance, for the future, a more detailed study of temperatures in the reservoir before expansion should be performed using a faster camera system. This would allow to exclude peak temperature loads during this phase of device operation.

6 APPENDIX

6.1 HEATER DESIGNS

6.1.1 MASK 1

Specifications	Mask Image	Simulated Heat Field
Heater 1 **s_{trace} = 75/100/125/150/150/150/ 150/125/100/75μm** **w_{trace} = 150μm**	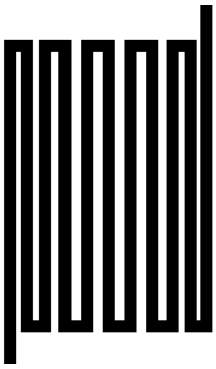	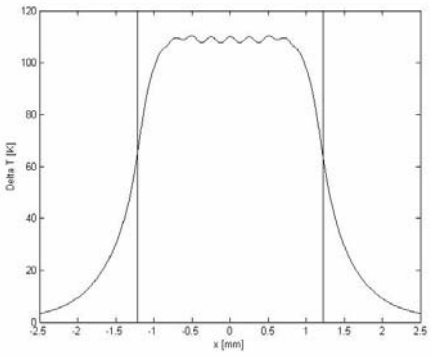
Heater 2 **s_{trace} = 100μm** **w_{trace} = 100/200/100μm**	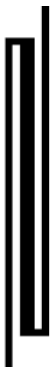	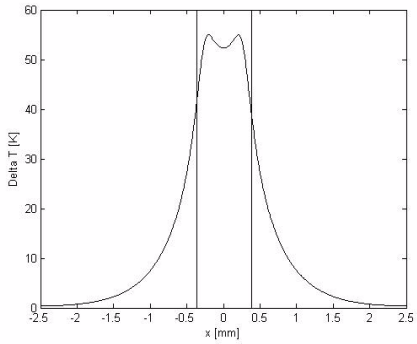
Heater 3 **s_{trace} = 100μm** **w_{trace} = 100/100/200/200/200μm**	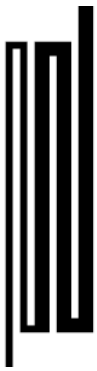	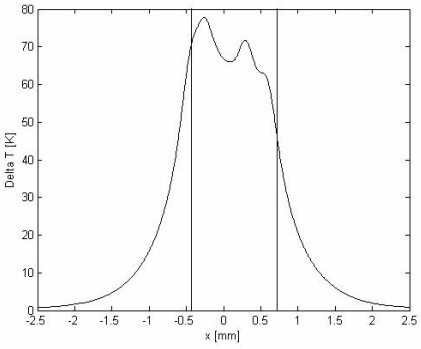

Table 6.1: *Heater designs, mask 1.*

Heater 4 “circular” **s_{trace} =** **75μm** **w_{trace} =** **100/225/250/275/300μm**		**(see mask 1, heater 8 for an estimate on the resulting profile in the heater midsection)**
Heater 5 **s_{trace} =** **75μm** **w_{trace} =** **200/275/275/275/300/275/275/275/200μm**	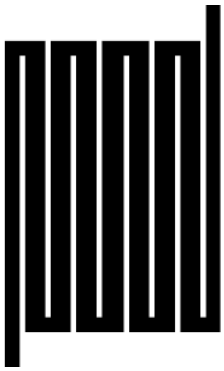	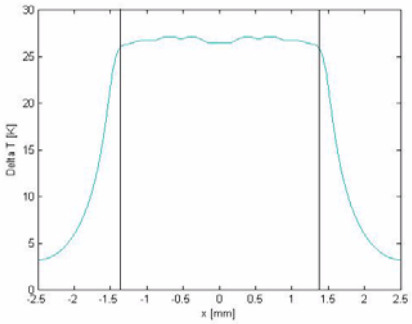
Heater 6 **s_{trace} =** **75μm** **w_{trace} =** **200/275/300/275/200μm**	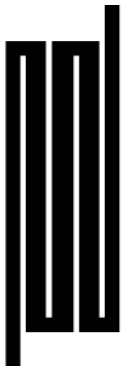	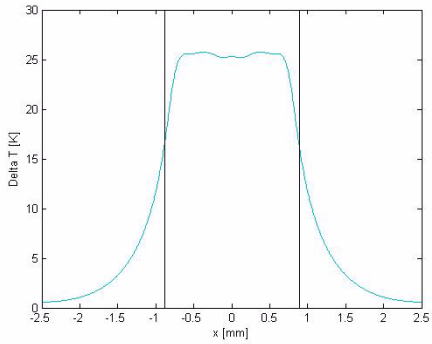

Table 6.1: *Heater designs, mask 1.*

Heater 7 **s_{trace} = 75μm** **w_{trace} = 200/275/275/300/275/275/200μm**	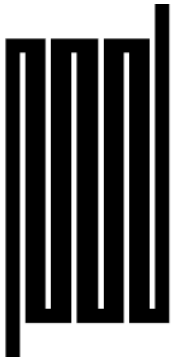	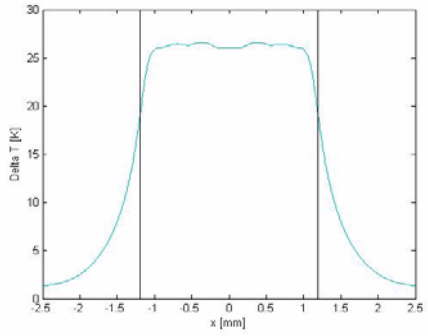
Heater 8 **s_{trace} = 75μm** **w_{trace} = 100/225/250/275/300μm**		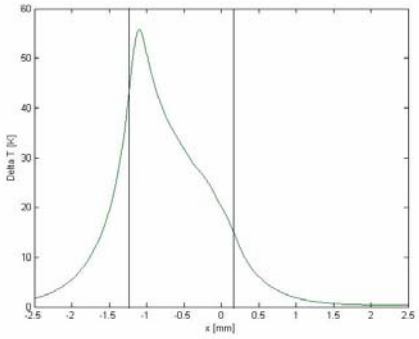

Table 6.1: *Heater designs, mask 1.*

6.1.2 MASK 2

Specifications	Mask Image	Simulated Heat Field
Heater 1 **s_{trace} = 75/95/125/145/145/145/145/125/95/75μm** **w_{trace} = 100μm**	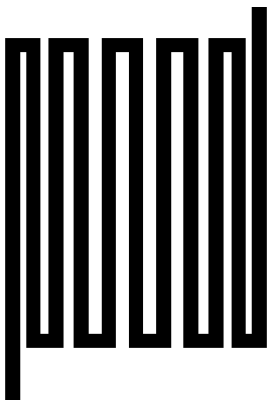	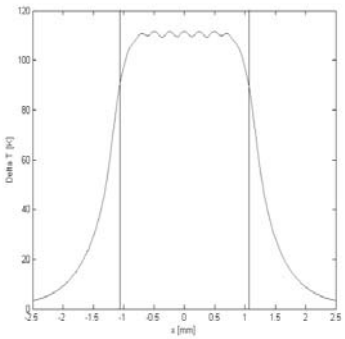

Table 6.2: *Heater designs, mask2.*

Heater 2 **s_{trace} = 75/125/115/105/95/85/75/ 75μm** **w_{trace} = 100μm**	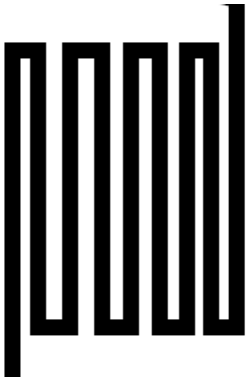	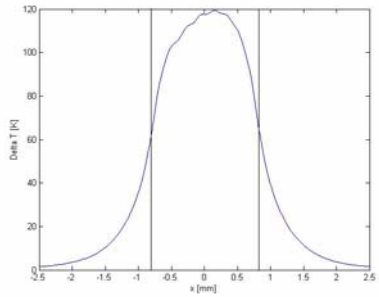
Heater 3 (see Mask 1)	-	-
Heater 4 **s_{trace} = 75/75/85/95/105/115/125/ 125μm** **w_{trace} = 100μm**	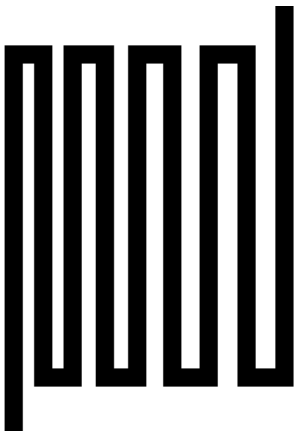	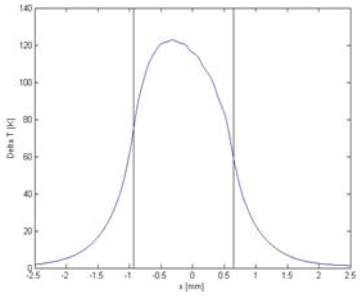
Heater 5 “square” (see Mask 1)	-	-
Heater 6 “square” (see Mask 1)	-	-
Heater 7 “square” (see Mask 1)	-	-
Heater 8 “square” (see Mask 1)	-	-

Table 6.2: *Heater designs, mask2.*

LabChip 1 **s_{trace} = 75/75/75/75/85/85/95/95/ 105/105/115/115/125/ 125μm** **w_{trace} = 100μm**	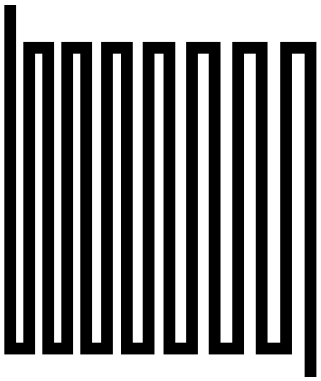	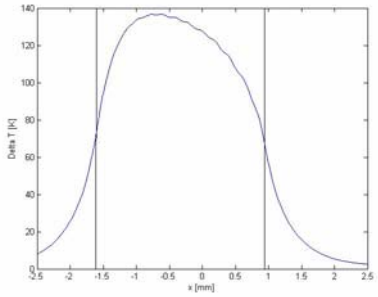
LabChip 2 **s_{trace} = 75μm** **w_{trace} = 100/100/225/225/250/250/ 275/275/300/300/300μm**	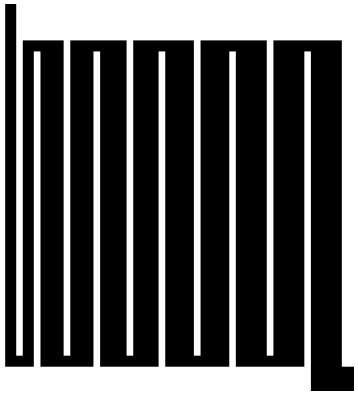	**(see mask 1, heater 8)**

Table 6.2: *Heater designs, mask2.*

6.2 MATLAB CODE - FLUORESCENCE-BASED THERMOMETRY

6.2.1 CALIBRATION

```
% Calibration of Fluorescence-based Thermometry
% 28102004, Volker Nock
% Nikon Eclipse ME600, RhodamineB 100umol/L PBS
% Matlab7

clear all; % clear all variables
 bg = imread('background281004.tif'); % read in background picture
 bg1= imresize(bg,[360 480]); % resize background image to image size
 a1 = imsubtract(imread('21_Image17.tif'),bg1); % read in image for 21°C, subtract background
 a2 = imsubtract(imread('25_Image17.tif'),bg1); % same as above but for 25°C
 a3 = imsubtract(imread('30_Image17.tif'),bg1);
 a4 = imsubtract(imread('35_Image17.tif'),bg1);
 a5 = imsubtract(imread('40_Image17.tif'),bg1);
 a6 = imsubtract(imread('44_Image17.tif'),bg1);
 a7 = imsubtract(imread('50_Image17.tif'),bg1);
 a8 = imsubtract(imread('55_Image17.tif'),bg1);
 a9 = imsubtract(imread('60_Image17.tif'),bg1);
 a10 = imsubtract(imread('65_Image17.tif'),bg1);
```

```
a11 = imsubtract(imread('70_Image17.tif'),bg1);
a12 = imsubtract(imread('75_Image17.tif'),bg1);
a13 = imsubtract(imread('80_Image17.tif'),bg1);
a14 = imsubtract(imread('85_Image17.tif'),bg1);
a15 = imsubtract(imread('90_Image17.tif'),bg1);
B1 = mean2(a1); % get average intensity for 21°C image
B2 = mean2(a2); % same as above for 25°C
B3 = mean2(a3);
B4 = mean2(a4);
B5 = mean2(a5);
B6 = mean2(a6);
B7 = mean2(a7);
B8 = mean2(a8);
B9 = mean2(a9);
B10 = mean2(a10);
B11 = mean2(a11);
B12 = mean2(a12);
B13 = mean2(a13);
B14 = mean2(a14);
B15 = mean2(a15);
B = [B1/B1 21; B2/B1 25; B3/B1 30; B4/B1 35; % create vector of relative intensity vs. temperature
    B5/B1 40; B6/B1 44; B7/B1 50; B8/B1 55; % with intensity normalized to 21°C
    B9/B1 60; B10/B1 65; B11/B1 70; B12/B1 75;
    B13/B1 80; B14/B1 85; B15/B1 90];
plotCalibration(B(:,2),B(:,1));  % plot intensity vs. temperature
plotCalibrationVS(B(:,2),B(:,1)); % plot temperature vs. intensity
```

plotCalibration

```
function plotCalibration(Bx,By)
figure(1)
subplot(1,1,1)
fresult1 = fit(Bx,By,'poly3')
h1 = plot(fresult1,'-r',Bx,By,'*b')
%set(k,{'LineWidth'},2)
%set(h,{'Marker'},{'o'})
%set(h,{'Color'},{'r'})
%axis([0 12 -0.5 1])
grid off
xlabel('Temperature [°C]')
ylabel('rel. Intensity')
legend(h1,'RhodamineB')
title('Calibration of Temperature-Dependent Fluorescence Microscopy (Nikon Eclipse ME600, 10x objective, 28/20/2004)')
```

plotCalibrationVS

```
function plotCalibrationVS(Bx,By)
figure(2)
subplot(1,1,1)
fresult2 = fit(By,Bx,'poly3')
```

```
h2 = plot(fresult2,'-r',By,Bx,'*b')
%set(k,{'LineWidth'},2)
%set(h,{'Marker'},{'o'})
%set(h,{'Color'},{'r'})
%axis([0 12 -0.5 1])
grid off
ylabel('Temperature [°C]')
xlabel('rel. Intensity')
legend(h2,'RhodamineB')
```

6.2.2 MEASUREMENT - HEATER CHARACTERIZATION

```
% Analysis of Fluorescence Images
% 02112004, Volker Nock
% Channel Structure over Heater, 10x, Nikon Eclipse ME600

clear all; %clear matlab workspace
bg021104 = imread('Background_Image4.tif');%read background image
A21_I0 = imsubtract(imread ('20_Image4.tif'),bg021104);%read image for I=0, T=21C, subtract Background
AT_I1 = imsubtract(imread('1_Image1.tif'),bg021104);%read image for I=1A, T=? ,subtract Background
AT_I03 = imsubtract(imread('0.3_Image1.tif'),bg021104);%read image for I=0.3A, T=? ,subtract Background
AT_I05 = imsubtract(imread('0.5_Image1.tif'),bg021104);%read image for I=0.5A, T=? ,subtract Background
AT_I08 = imsubtract(imread('0.8_Image1.tif'),bg021104);%read image for I=0.8A, T=? ,subtract Background
AT_I11 = imsubtract(imread('1.1_Image1.tif'),bg021104);%read image for I=1.1A, T=? ,subtract Background
AT_I12 = imsubtract(imread('1.2_Image1.tif'),bg021104);%read image for I=1.2A, T=? ,subtract Background
A21_I0_D = double(A21_I0); %convert to double format
BT_I1 = imdivide(double(AT_I1),A21_I0_D); %divide through image at T=21C
BT_I03 = imdivide(double(AT_I03),A21_I0_D);
BT_I05 = imdivide(double(AT_I05),A21_I0_D);
BT_I08 = imdivide(double(AT_I08),A21_I0_D);
BT_I11 = imdivide(double(AT_I11),A21_I0_D);
BT_I12 = imdivide(double(AT_I12),A21_I0_D);
x = [348 379 475 440 348]; %create mask to blind out all but channel
y = [1 600 600 1 1];
bw = poly2mask(x,y,600,800);
BT_I1_T = immultiply(fluorescenceFit(BT_I1),bw); %translate Intensity to Temperature, multiply with mask
BT_I11_T = immultiply(fluorescenceFit(BT_I11),bw);
BT_I12_T = immultiply(fluorescenceFit(BT_I12),bw);
BT_I03_T = immultiply(fluorescenceFit(BT_I03),bw);
BT_I05_T = immultiply(fluorescenceFit(BT_I05),bw);
BT_I08_T = immultiply(fluorescenceFit(BT_I08),bw);

% display results for different currents

figure(1)
subplot(3,2,1); ax1 = imshow(BT_I03_T);set(ax1,'CDataMapping','direct');
colormap hot;title('I=0.3A');colorbar('YTickLabel',...
   {'20°C','40°C','60°C','80°C','100°C','120°C'},'CLim',[20,150])
subplot(3,2,2); ax2 = imshow(BT_I05_T);set(ax2,'CDataMapping','direct');
colormap hot;title('I=0.5A');colorbar('YTickLabel',...
```

```
   {'20°C','40°C','60°C','80°C','100°C','120°C'},'CLim',[20,150])
subplot(3,2,3); ax3 = imshow(BT_I08_T);set(ax3,'CDataMapping','direct');
colormap hot;title('I=0.8A');colorbar('YTickLabel',...
   {'20°C','40°C','60°C','80°C','100°C','120°C'},'CLim',[20,150])
subplot(3,2,4); ax4 = imshow(BT_I1_T);set(ax4,'CDataMapping','direct');
colormap hot;title('I=1A');colorbar('YTickLabel',...
   {'20°C','40°C','60°C','80°C','100°C','120°C'},'CLim',[20,150])
subplot(3,2,5); ax5 = imshow(BT_I11_T);set(ax5,'CDataMapping','direct');
colormap hot;title('I=1.1A');colorbar('YTickLabel',...
   {'20°C','40°C','60°C','80°C','100°C','120°C'},'CLim',[20,150])
subplot(3,2,6); ax6 = imshow(BT_I12_T);set(ax6,'CDataMapping','direct');
colormap hot;title('I=1.2A');colorbar('YTickLabel',...
   {'20°C','40°C','60°C','80°C','100°C','120°C'},'CLim',[20,150])

% display 3D plot of temperature over channel for I=1.2A

figure(2)
F = imcrop(BT_I12_T,[340 1 160 800]);
mesh(F)
colormap jet
xlabel('x [pixel]');ylabel('y [pixel]');zlabel('T [°C]');title('Heat Field');
colorbar('YTickLabel',...
   {'20°C','40°C','60°C','80°C','100°C','120°C'})

% plot of temperature along channel

figure(3)
W = BT_I03_T(:,380:440); %create matrix corresponding with values in channel
F03 = mean(W,2) %average over width of channel
W = BT_I05_T(:,380:440);
F05 = mean(W,2)
W = BT_I08_T(:,380:440);
F08 = mean(W,2)
W = BT_I1_T(:,380:440);
F1 = mean(W,2)
W = BT_I11_T(:,380:440);
F11 = mean(W,2)
W = BT_I12_T(:,380:440);
F12 = mean(W,2)
plot([F12(:,1),F03(:,1),F05(:,1),F08(:,1),F1(:,1),F11(:,1)])
xlabel('x [pixel]');ylabel('T [°C]');title('Heat Field');
```

fluorescenceFit

```
% Matlab Function representing the Fluorescence-based Thermometry
% Calibration Curve Fit
% 03112004, Volker Nock
% T:temperature, I:intensity

function T = fluorescenceFit(I)
T = -85*I.^3+222*I.^2-246*I+130;
```

6.2.3 MEASUREMENT - ACTIVE DEVICES

```
% Analysis of Fluorescence Images
% 30122004, Volker Nock
% Channel End (transparent), 20x, Nikon Eclipse ME600

clear all; % clear matlab workspace

bg161104 = imread('Background30122004.tif'); % read background image
A21_I0 = imsubtract(imread ('Tx_t0005.tif'),bg161104); % T = room temperature, subtract background
[bw,xi,yi] = roipoly(A21_I0); % define channel mask
AT_1 = imsubtract(imread('Tx_t0007.tif'),bg161104); % read sequential images, subtract background
AT_2 = imsubtract(imread('Tx_t0008.tif'),bg161104);
AT_3 = imsubtract(imread('Tx_t0009.tif'),bg161104);
AT_4 = imsubtract(imread('Tx_t0010.tif'),bg161104);
AT_5 = imsubtract(imread('Tx_t0011.tif'),bg161104);
AT_6 = imsubtract(imread('Tx_t0012.tif'),bg161104);
AT_7 = imsubtract(imread('Tx_t0013.tif'),bg161104);
AT_8 = imsubtract(imread('Tx_t0014.tif'),bg161104);
AT_9 = imsubtract(imread('Tx_t0015.tif'),bg161104);
AT_10 = imsubtract(imread('Tx_t0016.tif'),bg161104);

A21_I0_D = double(A21_I0); % convert to double

BT_t0 = imdivide(double(AT_1),A21_I0_D); % divide through image at RT
BT_t1 = imdivide(double(AT_2),A21_I0_D);
BT_t2 = imdivide(double(AT_3),A21_I0_D);
BT_t3 = imdivide(double(AT_4),A21_I0_D);
BT_t4 = imdivide(double(AT_5),A21_I0_D);
BT_t5 = imdivide(double(AT_6),A21_I0_D);
BT_t6 = imdivide(double(AT_7),A21_I0_D);
BT_t7 = imdivide(double(AT_8),A21_I0_D);
BT_t8 = imdivide(double(AT_9),A21_I0_D);
BT_t9 = imdivide(double(AT_10),A21_I0_D);


BT_t0_T = immultiply(fluorescenceFit(BT_t0),bw); % apply channel mask and translate
BT_t1_T = immultiply(fluorescenceFit(BT_t1),bw); % intensity change into temperature
BT_t2_T = immultiply(fluorescenceFit(BT_t2),bw); % using routine fluorescenceFit
BT_t3_T = immultiply(fluorescenceFit(BT_t3),bw);
BT_t4_T = immultiply(fluorescenceFit(BT_t4),bw);
BT_t5_T = immultiply(fluorescenceFit(BT_t5),bw);
BT_t6_T = immultiply(fluorescenceFit(BT_t6),bw);
BT_t7_T = immultiply(fluorescenceFit(BT_t7),bw);
BT_t8_T = immultiply(fluorescenceFit(BT_t8),bw);
BT_t9_T = immultiply(fluorescenceFit(BT_t9),bw);

% display results for different sequential images

figure(1)
subplot(3,2,1); ax1 = imshow(BT_t0_T);set(ax1,'CDataMapping','direct');
```

```
colormap hot;title('0007');colorbar('YTickLabel',...
   {'20°C','40°C','60°C','80°C','100°C','120°C'},'CLim',[20,150])
subplot(3,2,2); ax2 = imshow(BT_t1_T);set(ax2,'CDataMapping','direct');
colormap hot;title('0008');colorbar('YTickLabel',...
   {'20°C','40°C','60°C','80°C','100°C','120°C'},'CLim',[20,150])
subplot(3,2,3); ax3 = imshow(BT_t2_T);set(ax3,'CDataMapping','direct');
colormap hot;title('0009');colorbar('YTickLabel',...
   {'20°C','40°C','60°C','80°C','100°C','120°C'},'CLim',[20,150])
subplot(3,2,4); ax4 = imshow(BT_t3_T);set(ax4,'CDataMapping','direct');
colormap hot;title('0010');colorbar('YTickLabel',...
   {'20°C','40°C','60°C','80°C','100°C','120°C'},'CLim',[20,150])
subplot(3,2,5); ax5 = imshow(BT_t4_T);set(ax5,'CDataMapping','direct');
colormap hot;title('0011');colorbar('YTickLabel',...
   {'20°C','40°C','60°C','80°C','100°C','120°C'},'CLim',[20,150])
subplot(3,2,6); ax6 = imshow(BT_t5_T);set(ax6,'CDataMapping','direct');
colormap hot;title('0012');colorbar('YTickLabel',...
   {'20°C','40°C','60°C','80°C','100°C','120°C'},'CLim',[20,150])

figure(2)
subplot(3,2,1); ax1 = imshow(BT_t6_T);set(ax1,'CDataMapping','direct');
colormap hot;title('0013');colorbar('YTickLabel',...
   {'20°C','40°C','60°C','80°C','100°C','120°C'},'CLim',[20,150])
subplot(3,2,2); ax2 = imshow(BT_t7_T);set(ax2,'CDataMapping','direct');
colormap hot;title('0014');colorbar('YTickLabel',...
   {'20°C','40°C','60°C','80°C','100°C','120°C'},'CLim',[20,150])
subplot(3,2,3); ax3 = imshow(BT_t8_T);set(ax3,'CDataMapping','direct');
colormap hot;title('0015');colorbar('YTickLabel',...
   {'20°C','40°C','60°C','80°C','100°C','120°C'},'CLim',[20,150])
subplot(3,2,4); ax4 = imshow(BT_t9_T);set(ax4,'CDataMapping','direct');
colormap hot;title('0016');colorbar('YTickLabel',...
{'20°C','40°C','60°C','80°C','100°C','120°C'},'CLim',[20,150])

% display average temperature over channel

figure(3)
F0 = channelAverage(BT_t0_T); % average over width of channel using
F1 = channelAverage(BT_t1_T); % routine channelAverage
F2 = channelAverage(BT_t2_T);
F3 = channelAverage(BT_t3_T);
F4 = channelAverage(BT_t4_T);
F5 = channelAverage(BT_t5_T);
F6 = channelAverage(BT_t6_T);
F7 = channelAverage(BT_t7_T);
F8 = channelAverage(BT_t8_T);
F9 = channelAverage(BT_t9_T);
plot([F0(:,1),F1(:,1),F2(:,1),F3(:,1),F4(:,1),F5(:,1),...
   F6(:,1),F7(:,1),F8(:,1),F9(:,1)])
xlabel('x [pixel]');ylabel('T [°C]');title('Heat Field');
```

channelAverage

```
% function channelAverage
% takes a matrix A and averages
% all row elements not zero
% gives back a vector of row average
% 18.11.2004, Volker Nock

function T = channelAverage(A)
[m,n] = size(A);
B=zeros(m,1);

for y = 1:m
   l=0;
   Z=0;
   for x = 1:n
     if A(y,x)>0
        Z = Z+A(y,x);
        l=l+1;
     end
   end
   if Z>0
      B(y)=Z/l;
   else
      B(y)=0;
   end
end
T=B;
```

7 LIST OF SYMBOLS

Symbol	Description
s_{trace}	trace spacing
ω_r	heater width
d_{sub}	substrate thickness
d_{trace}	trace thickness
l_{trace}	trace length
w_{trace}	trace width
P	power
σ	electrical conductivity
Q	heat
ρ	density
V	voltage
$\rho_{el,RT}$	electrical resistivity at room temperature
C_p	thermal capacity
k	thermal conductivity
T	temperature
T_{inf}	ambient temperature
α	temperature coefficient of resistivity
t	time
n	normal vector
I	current
R_{el}	electrical resistance
j_0	current density
IFL	fluorescence intensity
IFL,0	fluorescence excitation intensity
C	concentration
A	fraction available light collected
L	sampling length along the incident beam
ϵ	molar absorptivity

Table 7.3: *List of physical symbols and constants used in the thesis.*

Symbol	Description
ϕ	quantum yield
σ_{SB}	Stefan-Boltzmann constant
ϵ_{em}	surface emissitivity

Table 7.3: *List of physical symbols and constants used in the thesis.*

ACKNOWLEDGMENTS

In looking back, writing this thesis was as much about the work contained within it, as it probably was about the people that helped and supported me during my time at the Microsystem Lab at KTH. To all of you I would hereby like to express my gratitude and say thank you for an inspiring experience.
In particular I am indebted to the following people:

Prof. Dr. Göran Stemme, my examiner, for giving me the opportunity to work in his microsystem laboratory.

Prof. Dr.-Ing. Peter Woias, my co-examiner, for being my supervisor for IMTEK and his help in arranging the organizational part in Germany.

My supervisor Dipl.-Ing. Björn Samel for being the perfect combination of friend and teacher, as well as his excellent support, inspiration and guidance in the wonderful world of microfluidics and expandable microspheres.

Prof. Haviland and Jessica Hultström for help with the fluorescence microscope.

All the members of the microsystem lab: Anna, Elizabeth, Laurent, Ruifeng, Hans, Joachim, Wouter, Stefan, Sjoerd, Aman, Niclas, Thomas, Frank, Jessica, Carl-Gunnar and Kjell for a great time and all the invaluable help.

My parents, Alice and Hans Nock, for their love and support through all the times and all the countries.

And finally, my partner Lisa, for her love and for giving me a second home in her beautiful country.

9 REFERENCES

[1] M. Engler, N. Kockmann, T. Kiefer, P. Woias, “Numerical and experimental investigations on liquid mixing in static micromixers”, *Chemical Engineering Journal (2004)*, Vol. 101, pp. 315-322

[2] J. Melin, G. Gimenez, N. Roxhed, W. van der Wijngaart, G. Stemme, “A Passive 2-Dimensional Liquid Sample Micromixer”, *Proceedings of the 7th international conference on Micro Total Analysis Systems (MicroTAS 2003)*, Squaw Valley, USA, pp. 167-171.

[3] A. Russom, S. Haasl, A. Ohlander, T. Mayr, A. J. Brookes, H. Andersson, G. Stemme, “Genotyping by Dynamic Heating of Monolayered Beads on a Microheater Surface”, *Proceedings of mTAS 2004, 8th International Conference on Miniaturized Systems in Chemistry and Life Sciences (2004)*, Vol. 2, pp. 303-305.

[4] T. O. Herndon, S. Gonzalez, T. R. Gowrishankar, R. R. Anderson, “Transdermal microconduits by microscission for drug delivery and sample acquisition”, *BMC Medicine (2004)*, 2:12, BioMed Central.

[5] PassPort™ System, *www.alteatherapeutics.com*, Altea Therapeutics, Tucker, USA.

[6] P. Griss, G. Stemme, “Side-Opened Out-of-Plane Microneedles for Microfluidic Transdermal Liquid Transfer”, *Journal of Microelectromechanical Systems (2003)*, Vol. 12, No. 3, pp. 296-301.

[7] C.-C. Hong, S. Murugesan, S. Kim, G. Beaucage, J.-W. Choi, C. H. Ahn, “A functional on-chip pressure generator using solid chemical propellant for disposable lab-on-a-chip”, *Lab on a Chip (2003)*, Issue 3, pp. 281-286.

[8] C.-C. Hong, J.-W. Choi, C. H. Ahn, “Disposable Air-Busting Detonators as an Alternative On-Chip Power Source”, *Technical Digest. MEMS 2002 IEEE International Conference. 15th IEEE International Conference on Micro Electro Mechanical Systems (2002)*, pp. 240-243.

[9] Y. H. Choi, S. Son, S. S. Lee, “Novel Micropump using Oxygen as Pumping Source”, *Technical Digest. MEMS 2003 IEEE International Conference. 16th IEEE International Conference on Micro Electro Mechanical Systems (2003)*, pp. 116-119.

[10] Expancel Microspheres, “An Introduction”, *www.expancel.com*

[11] Expancel DU, “Product Specification”, *www.expancel.com*

[12] P. Griss, H. Andersson, and G. Stemme, “Liquid handling using expandable microspheres”, in *Technical Digest. MEMS 2002 IEEE International Conference. 15th*

IEEE International Conference on Micro Electro Mechanical Systems (2002), pp. 117-120.

[13] H. Andersson, P. Griss, G. Stemme, "Expandable Microspheres - surface immobilization techniques", *Sensors and Actuators B (2002)*, Vol. 84, pp. 290-295.

[14] S. Rydholm, "Expandable microspheres for liquid actuation and dosing", *Master's Thesis, Royal Institute of Technology, Dept. of Signals, Sensors and Systems*, March 2003.

[15] N. Roxhed, S. Rydholm, B. Samel, W. van der Wijngaart, P. Griss, G. Stemme, "Low Cost Device For Precise Microliter Range Liquid Dispensing", in *Technical Digest. MEMS 2004 IEEE International Conference. 17th IEEE International Conference on Micro Electro Mechanical Systems (2004)*, pp. 326-329.

[16] S. Balslev, N. Roxhed, P. Griss, G. Stemme, A. Kristensen, "Microfluidic Dye Laser with Compact, Low-cost Liquid Dye Dispenser", *Proceedings of mTAS 2004, 8th International Conference on Miniaturized Systems in Chemistry and Life Sciences (2004)*, Vol. 2, pp. 375-377.

[17] B. Samel, P. Griss, G. Stemme, "Expandable Microspheres incorporated in a PDMS Matrix: A Novel Thermal Composite Actuator for Liquid Handling in Microfluidic Applications", in *Transducers'03 The 12th International Conference on Solid-State Sensors, Actuators and Microsystems*, pp. 1558-1561.

[18] P. Griss, G. Stemme, "Side-Opened Out-of-Plane Microneedles for Microfluidic Transdermal Liquid Transfer", *IEEE Journal of Microelectromechanical Systems*, Vol. 12, No. 3, pp. 296-301.

[19] B. Samel, J. Melin, P. Griss, G. Stemme, "Single-use microfluidic pumps and valves based on thermally responsive PDMS composite", *MEMS 2005 IEEE International Conference. 18th IEEE International Conference on Micro Electro Mechanical Systems (2005)*, accepted.

[20] C. F. Coombs, Jr., "Printed Circuits Handbook", 4th. edition, McGraw-Hill, New York, 1996.

[21] I. Moser, G. Jobst, P. Svasek, M. Varahram, G. Urban, "Rapid liver enzyme assay with miniaturized liquid handling system comprising thin film biosensor array", *Sensors and Actuators (1997)*, B 44, pp. 377-380.

[22] A. Wego, S. Richter, L. Pagel, "Fluidic microsystems based on printed circuit board technology", *Journal of Micromechanics and Microengineering (2001)*, Vol. 11, pp. 528 -531.

[23] A. P. Sudarsan, V. M. Ugaz, “Printed Circuit Technology for Fabrication of Plastic-Based Microfluidic Devices”, *Analytical Chemistry (2004)*, Vol. 76, pp. 3229-3235.

[24] C. Li, C. N.Cheung, J. Yang, C. H. Tzang, M. Yang, “PDMS-based microfluidic device with multi-height structures fabricated by single-step photolithography using printed circuit board as masters”, *The Analyst (2003)*, Vol. 128, pp. 1137-1142.

[25] J. Adam, “New Correlations Between Electrical Current and Temperature Rise in PCB Traces”, in *Proceedings of the 20th IEEE SEMI-THERM Symposium (2004)*, San Jose, CA, March 2004.

[26] A. A. Darhuber, S. M. Troian, “Generation of high-resolution surface temperature distributions”, *Journal of Applied Physics (2002)*, Vol. 91, No. 9, pp. 5685-5693.

[27] Documentation FEMLAB 3.0a, Comsol AB, Stockholm, Sweden.

[28] R. D. Weinstein, A. S. Fleischer, K. A. Krug, “Natural Convection and Passive Heat Rejection from Two Heat Sources Maintained at Different Temperatures on a Printed Circuit Board”, *Transactions of the ASME (2004)*, Vol. 126, pp.14-21.

[29] www.goodfellow.com, Goodfellow SARL, Lille, France.

[30] http://web.mit.edu/6.777/www/matprops/matprops.htm, Material Properties Database, Department of Electrical Engineering and Computer Design, MIT, Cambridge, USA

[31] B. Samel, V. Nock, A. Russom, P. Griss, G. Stemme, “Nanoliter Liquid Handling On A Low Cost Disposable With Embedded Fluid Actuators”, submitted to *Transducers’05 The 13th International Conference on Solid-State Sensors, Actuators and Microsystems*.

[32] D. Ross, M. Gaitan, L. E. Locascio, “Temperature Measurement in Microfluidic Systems Using a Temperature-Dependent Fluorescent Dye”, *Analytical Chemistry (2001)*, Vol. 73, No. 17, pp. 4117-4123.

[33] D. Ross, L. E. Locascio, “Microfluidic Temperature Gradient Focusing”, *Analytical Chemistry (2002)*, Vol. 74, No. 11, pp. 2556-2564.

[34] D. Erickson, D. Sinton, D. Li, ”Joule heating and heat transfer in poly(dimethylsiloxane) microfluidic systems”, *Lab on a Chip (2003)*, Issue 3, pp. 141-149.

[35] X. Xuan, B.Xu, D. Sinton, D. Li, “Electroosmotic flow with Joule heating effects”, *Lab on a Chip (2004)*, Issue 4, pp. 230-236.

[36] J. Sakakibara, K. Hishida, M. Maeda, ”Measurements of Thermally Stratified Pipe Flow using Image Processing Techniques”, *Experiments in Fluids (1993)*, Vol. 16, pp. 82-96.

[37] J. Ferguson, A. W.-H. Mau, “Spontaneous and stimulated emission from dyes. Spectroscopy the neutral molecules of acridine orange, proflavine, and rhodamine B“, *Australian Journal of Chemistry (1973)*, Vol. 26, pp. 1617-24.

[38] M. Madou, “Fundamentals of Microfabrication”, 1. edition, CRC Press, Boca Raton, 1997